

Probing of Pressure-Induced Bonding Transitions in Crystalline and Amorphous Earth Materials: Insights from X-ray Raman Scattering at High Pressure

Sung Keun Lee

*School of Earth and Environmental Sciences
Seoul National University, Seoul, 151-742 Korea*

sungkle@snu.ac.kr

Peter J. Eng

*Consortium for Advanced Radiation Sources
and*

James Franck Institute

University of Chicago, Chicago, Illinois 60637, U.S.A.

Ho-kwang Mao

Geophysical Laboratory

Carnegie Institution of Washington, Washington D.C., 20015, U.S.A.

*Center for High Pressure Science and Technology Advanced Research
1690 Cailun Rd., Pudong, Shanghai 201203, P.R. China*

INTRODUCTION

Knowledge of the electronic structure of crystalline and non-crystalline earth materials at ambient and high pressure are essential in order to understand the atomic origins of electronic, thermodynamic, and mechanical properties of these materials in the Earth's crust as well as Earth and planetary interiors (Hemley 1998; Laudernet et al. 2004; Stixrude and Karki 2005; Mao and Mao 2007; Price 2007; Stixrude 2007). Pressure-induced changes in the electronic structure of crystalline and amorphous silicates and oxides (glasses and melts) with low-*z* elements (e.g., Si, O, B, Li, C, etc.) have implications for diverse geophysical and magmatic processes relevant to the evolution and differentiation of the earth (e.g., mantle convection and mantle melting) (Stebbins 1995; Wolf and McMillan 1995; Lee 2005, 2011; Mysen and Richet 2005; Murakami and Bass 2010). Despite this importance, the analysis of the effect of pressure on the electronic structure and the nature of bonding in the crystalline and, particularly, non-crystalline oxides has remained one of the challenging problems in mineral physics and geochemistry, as well as, condensed matter physics. This is mostly because of the lack of suitable experimental probes of electronic bonding around these light elements in the earth materials under pressure.

Advances in *in situ* high pressure technologies, together with progress in X-ray optics in synchrotron radiation and first principle calculations have revealed structural details of bonding transitions of crystalline earth materials at high pressure (Hemley 1998; Mao and Mao 2007; Price 2007; Stixrude 2007). The non-resonant synchrotron inelastic X-ray scattering (NRIXS, also known as X-ray Raman, XRS) is one of the relatively new synchrotron X-ray probes of local structures with element-specificity. It explores the electronic bonding transitions in soft X-ray absorption edges using hard X-rays (e.g., ~ 10 keV) by tuning the energy loss (energy

of incident X-rays – energy of scattered X-rays) to the binding energy of electrons in elements of interest (Mao et al. 2003, 2006, 2010; Schulke 2007; Lee et al. 2008b; Rueff and Shukla 2010). Progress in XRS has been combined with advances in *in situ* high pressure technology and consequently, in the last 6-7 years it has been possible to examine the detailed pressure-induced electronic bonding transitions in low-*z* oxide glasses, molecules, and crystals by tuning the *K*-edges of elements in the 2nd row of the periodic table and/or to the *L-M* edges of heavier elements both at ambient and at high pressure (e.g., Schulke 2007; Rueff and Shukla 2010). The observed XRS results for amorphous oxides under compression contribute to the understanding of the atomistic origins of anomalous changes in melt properties in the Earth's interiors.

While the following list is by no means complete, important classes of materials studied by XRS at ambient pressure include Li, LiC₆, LiF, Li₃N, Li-borate glass, phases used for Li-batteries, and Li-peroxide (with Li *K*-edge) (Schulke et al. 1991, 1986; Krisch et al. 1997; Nagasawa et al. 1997; Hamalainen et al. 2002; Fister et al. 2008a, 2011b; Chan et al. 2011; Karan et al. 2012), Be crystals and BeO (with Be *K*-edge) (Schulke et al. 1986; Nagasawa et al. 1989). The C *K*-edge was used to explore bonding details of graphite (Tohji and Udagawa 1987; Schulke et al. 1988; Nagasawa et al. 1989), carbon in diverse aromatic rings, C₆₀ (Rueff et al. 2002; Gordon et al. 2003), and hydrocarbons (Feng et al. 2008; Fister et al. 2008b; Sakko et al. 2011). B *K*-edge XRS has provided structural details of BN (Watanabe et al. 1996), B₂O₃, Na-, and Li-borate glasses (Lee et al. 2005, 2007, 2008a). The utility of O-*K* edge XRS has been demonstrated in the study of H₂O and its polymorphs (Bowron et al. 2000; Bergmann et al. 2002b; Wernet et al. 2004, 2005; Cai et al. 2005; Tse et al. 2008; Fister et al. 2009). Oxygen environments of oxide glasses (SiO₂, B₂O₃, GeO₂, alkali borate glasses, and MgSiO₃) and silicate crystals (SiO₂, MgSiO₃) have also been investigated using XRS (Lin 2007; Lee et al. 2008a, 2005, 2007, 2008b; Fukui et al. 2009a; Lelong et al. 2012; Yi and Lee 2012). Recently, Na *K*-edge XRS provided the core-electron excitation spectra for NaF and NaCl (Nagle et al. 2009). Application of XRS has been extended to the characterization of oxide thin films (Fister et al. 2011a).

XRS can be particularly effective in studying the electronic structure at high pressure and has been used to yield the electronic structure of helium (He *K*-edge) (Mao et al. 2010), carbon polymorphs (graphite, diamond, amorphous carbon, C *K*-edge) (Mao et al. 2003; Lin et al. 2011), BN (with boron *K*-edge) (Meng et al. 2004), dense oxygens (Meng et al. 2008), H₂O polymorphs (O *K*-edge) (Cai et al. 2005; Tse et al. 2008), and oxide glasses under static compression (see the “*Pressure-Induced Structural Changes in Crystalline and Amorphous Earth Materials: Insights from X-ray Raman Scattering*” section below). Because the features in XRS spectra are sensitive to local “short-range” structure, the technique has been particularly useful in revealing structural changes in non-crystalline oxides at high pressure (Lee et al. 2005; Lin 2007; Fukui et al. 2009a; Lelong et al. 2012). For instance, B *K*-edge XRS studies of borate glasses at high pressure showed the first unambiguous experimental evidence for the formation of highly coordinated boron (i.e., [⁴B] at high pressure (Lee et al. 2005, 2007, 2008a). O *K*-edge XRS studies of diverse low-*z* oxide glasses suggested the pressure-induced increases in the fraction of triply coordinated oxygen associated with cation coordination changes (Lin 2007; Lee et al. 2008b, 2012; Lelong et al. 2012). Topological disorder also tends to increase with pressure as shown by the increase in the width of the O *K*-edge feature with pressure (Lee et al. 2008b). The O *K*-edge XRS of shock compressed multi-component quaternary oxide glasses showed evidence for the topologically driven densification in model basaltic glasses. This has strong geochemical implications for impact processes (Lee et al. 2012). Atomic configurations around network modifying cations in alkali silicate glasses were explored using Li *K*-edge XRS (Lee et al. 2007).

In addition to *K*-edges of low-*z* elements, XRS technique has also been useful to probe the edge features for loosely bound electrons in earth materials (e.g., *L*- and *M*- and higher

edges) (see the “*Remaining Challenges and Outlook: Applications of New K-, L-, M-edge XRS, XRS with Momentum Transfer, In Situ High Temperature and Pressure XRS Study for Multi-Components Glasses*” section for further details). These examples showed that XRS is beneficial for revealing the rich information of electron bonding transitions surrounding low- z elements in diverse crystalline and non-crystalline solids at 1 atm that are traditionally difficult to explore using other conventional techniques.

In this chapter, we provide an overview of the recent progress and insights provided by XRS on the electronic structure of key earth materials. Particular emphasis will be placed on the pressure-induced bonding transitions in dense molecules and non-crystalline oxides. We note that excellent accounts of earlier studies on fundamentals of XRS can be found in the previous review (Schulke 2007). The general application of IXS technique at high pressure (including that of XRS) can also be found in the previous reviews (Schulke 2007; Rueff and Shukla 2010). Short but helpful reviews of XRS techniques with experimental setups can also be found in (Bergmann et al. 2002a, 2004; Fister et al. 2006). There are also extensive reviews and discussion of O K -edge studies of H_2O polymorphs and thus these will not be discussed in detail here (e.g., Bowron et al. 2000; Bergmann et al. 2002b; Wernet et al. 2004; Cai et al. 2005; Tse et al. 2005, 2008; Fister et al. 2009). In the current chapter, we first outline the brief theoretical principles of X-ray Raman spectroscopy and experimental setups required for XRS measurement at high pressure. We then present the recent XRS results of the electronic bonding transitions in earth materials. A brief account of theoretical calculations of XRS spectra for mantle minerals is also presented. We also present several new XRS spectra for $CaSiO_3$ glass at ambient and high pressure in order to demonstrate the utility of XRS. Finally, we discuss the future challenges in exploring the structure of diverse earth materials at high pressure using XRS spectroscopy.

BRIEF REMARKS ON THEORETICAL BACKGROUNDS AND XRS EXPERIMENTS AT HIGH PRESSURE

Brief theoretical backgrounds

Recent advances in synchrotron X-ray optics, multi-element IXS analyzers specifically for XRS experiments, and improved diamond anvil cells (DACs) have revealed previously unknown details of the atomic configurations of crystalline materials at high pressure. Although detailed theoretical backgrounds and principles of inelastic X-ray scattering (IXS) can be found in recent reviews and textbooks (Schulke 2007; Rueff and Shukla 2010), brief theoretical background of non-resonant (NR) IXS is presented to provide the necessary information to understand the advantages (and disadvantages) of the method.

In the XRS process, the intensity of inelastically scattered photons is estimated with varying scattering angle (2θ) (and thus momentum transfer, $q = k_1 - k_2$) (Fig. 1). Energy loss (ΔE) in the process is achieved from the difference between energy of incident X-ray photon (E_{ins}) and scattered X-ray photon (E_{scat}). Spectra are collected by varying E_{ins} (with a monochromator) at a fixed analyzer energy of E_{scat} . The experimental measurable in the above process is the non-resonant double differential scattering cross section (DDSCS) of X-ray and is defined as a change in number of scattered photons (σ) with respect to changes in solid angle (Ω_2) and frequency of scattered photon (ω_2) as shown below (Fourier transform of the DDSCS results in electron density as a function of time and spatial coordinates):

$$\frac{d^2\sigma}{d\Omega_2 d\omega_2} = r_0^2 \left(\frac{\omega_2}{\omega_1} \right) |\varepsilon_1 \cdot \varepsilon_2|^2 S(q, \omega) \quad (1)$$

where r_0 is classical electron radius ($= e^2/mc^2$) and $S(q, \omega)$ is dynamic structure factor, which

X-ray Raman Scattering Process in Diamond Anvil Cell

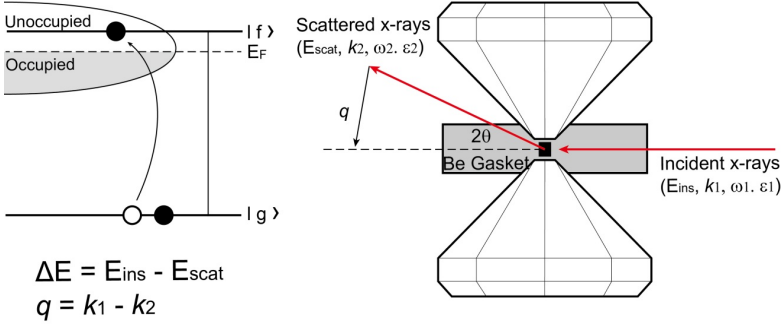


Figure 1. X-ray Raman scattering processes in a diamond anvil cell. E_{ins} , k_1 , ω_1 , and ϵ_1 are energy, wave vector, frequency, and polarization vector of the incident photon, respectively. E_{scat} , k_2 , ω_2 , and ϵ_2 are those for the scattered photon. $|g\rangle$ and $|f\rangle$ are the initial and final electronic states. E_F is the Fermi energy.

can be expressed as shown below:

$$S(q, \omega) = \sum_{g,f} \left| \langle f | e^{iq \cdot r} | g \rangle \right|^2 \delta(E_g - E_f + \hbar\omega) \quad (2)$$

where g and f denote ground and final states and E_g and E_f are electronic energy levels of the ground and final states, respectively (Fig. 1) and thus $\langle f | e^{iq \cdot r} | g \rangle$ is the transition matrix that shows the correlation between the ground and excited states. The non-resonant scattering cross section is thus shown below:

$$\frac{d^2\Omega}{d\Omega_2 d\omega_2} = \left(\frac{d\sigma}{d\Omega_2} \right)_{Th} \sum_{g,f} \left| \langle f | e^{iq \cdot r} | g \rangle \right|^2 \delta(E_g - E_f + \hbar\omega) \quad (3)$$

where Thomson scattering by a free electron is defined below:

$$\left(\frac{d\sigma}{d\Omega_2} \right)_{Th} = r_0^2 \left(\frac{\omega_2}{\omega_1} \right) \left| \epsilon_1 \cdot \epsilon_2 \right|^2 \quad (4)$$

In the non-resonant IXS process relevant to X-ray Raman Scattering (XRS), the incident energy (~ 10 keV) is much larger than the binding energy (less than 1 keV for low- z elements) of core electrons. At small scattering angle, $q \cdot r$ is much smaller than 1 ($\ll 1$), and the transition matrix can thus be approximately described by:

$$\langle f | e^{iq \cdot r} | g \rangle \cong \langle f | g \rangle + i \langle f | q \cdot r | g \rangle - 1/2 \langle f | (q \cdot r)^2 | g \rangle + \dots \quad (5)$$

Assuming orthogonality of initial and final state wave functions ($\langle f | g \rangle = 0$), the first order term is dominant and the resulting double differential scattering cross section can be described below:

$$\frac{d^2\Omega}{d\Omega_2 d\omega_2} = \left(\frac{d\sigma}{d\Omega_2} \right)_{Th} \sum_{g,f} \left| \langle f | r | g \rangle \right|^2 \delta(E_g - E_f + \hbar\omega) \quad (6)$$

As shown in Equation (6) above, under the dipole transition selection rule, the transition matrix for the XRS cross section at low scattering vector (i.e., $\langle f | r | g \rangle$) is identical to that of XAS, thus providing identical spectra to X-ray absorption near-edge structure (XANES) spectra (see Schulke 2007; Rueff and Shukla 2010; Henderson et al. 2014, this volume for

a review). In addition, with increasing momentum transfer, q (and thus scattering angle), transitions from non-dipole contributions can also be observed. Higher order terms in Equation (6) (e.g., $\langle f | (q \cdot r)^2 | g \rangle$) can be prevalent and the bonding nature relevant to momentum transfer (q -dependence) during the IXS process can be examined (Mizuno and Ohmura 1967; Suzuki 1967; Tohji and Udagawa 1987, 1989; Bergmann et al. 2000) (see the section “*Comparison with other core-electron excitation spectroscopy and traditional experimental probes at high pressure*” below for brief remarks on previous studies of q -dependence in XRS spectrum). With high brilliance synchrotron hard X-rays (~ 10 keV), XRS allows us to probe the configurations around low- z element (typically from He to Na K -edges) of diverse materials (as well as high L and M edges of third and fourth elements) without using an ultrahigh vacuum environment, yielding bulk sensitivity with resolution of XAS.

Comparison with other core-electron excitation spectroscopy and traditional experimental probes at high pressure

Comparison with other core-electron excitation spectroscopy. Local electronic bonding structure with the transition matrix, $\langle f | r | g \rangle$ in Equation (6) can be obtained using several experimental techniques that probe the energy-loss near-edge structure (ELNES) of the elements of interest stemming from an excitation of core (or valence) electron to unbound states (Fig. 1). These techniques unveil element-specific electronic bonding environments (i.e., local atomic structures, bonding nature, coordination number, and chemical environments) around atoms of interest. One of the popular techniques is X-ray absorption spectroscopy [XAS, either X-ray absorption near-edge structure (XANES) and extended X-ray absorption fine structure (EXAFS)] (see Newville 2014, this volume; Henderson et al. 2014, this volume). Additionally, electron scattering techniques using transmission electron microscopy (TEM) offer electron energy loss spectroscopy (EELS), yielding spectral response function with identical transition matrix elements (e.g., see Brown et al. 1995; de Groot 2001; Wilke et al. 2001; Stohr 2003; Brydson et al. 2014, this volume and references therein). XRS compliments these established techniques involving excitation of core and/or valence electrons into unoccupied electronic states.

Whereas the local electronic bonding natures of low- z glasses and crystals at ambient pressures have been extensively studied using soft X-ray XANES spectroscopy (e.g., Seifert et al. 1996; Wu et al. 1996; Garvie et al. 2000; Henderson et al. 2009), application of XAS is often more suitable for high- z elements using hard X-ray because its application to soft X-ray region requires vacuum conditions (used to minimize the scattering from air molecules). Furthermore, conventional synchrotron XAS may not be suitable for probing low- z oxides at high pressures due to the inability of the soft X-rays to penetrate the sample environments to sustain its high pressure condition (e.g., Be gasket of a diamond anvil cell). Due to limited penetration depth of the soft X-ray photon for low- z element XAS, XAS of these elements is often more suitable for probing of surface structure. While the EELS technique can be potentially useful for studying quenched materials (compressed and decompressed within a DAC) and to probe electronic excitations of low- z elements, it suffers limitations in its *in situ* investigation of electronic bonding transitions in oxide materials at high pressure as *in situ* high pressure techniques cannot be combined with TEM. Furthermore, the electron beam during sample preparation and measurement may alter the sample. In summary, X-ray Raman scattering (XRS) is one of the non-resonant inelastic X-ray techniques and is obtained using hard X-rays. XRS is thus an element-specific (tuning with electron binding energy), *in situ* experimental probe of bulk oxides with low- z elements at extreme conditions (and at ambient pressure) using hard X-rays. It provides sensitivity similar to that of soft X-rays (similar transition matrix for scattering cross section); therefore, it allows us to probe the detailed local bonding nature of low- z elements in crystalline and amorphous oxides, molecular solids, and liquids *in situ* at high pressures (Bergmann et al. 2002a; Mao et al. 2003; Wernet et al. 2004; Cai et al. 2005; Lee et al. 2005b, 2007, 2008b, 2008b; Lin et al. 2007; Schulke 2007; Meng et al. 2008, 2004; Fukui et al. 2009; Rueff and Shukla 2010).

As an example of the utility and uniqueness of XRS at 1 atm, Figure 2 shows typical IXS spectra for CaSiO_3 glass at 1 atm. The elastic X-ray signal is dominant at an energy loss (i.e., energy difference between incident energy and elastic energy) of 0 eV. The broad feature at ~ 10 -140 eV is due to the Compton scattering peak. The Compton scattering peak position moves to higher energy and the Compton peak width also gets broader with increasing scattering angle (2θ). The spectra also show the first experimental results for Ca M -edge features [Ca $M_{2,3}$ (from Ca $3p$ state to an unbound state) at energy loss of ~ 28 eV and Ca M_1 (Ca $3s$ state to an unbound state) edge at ~ 45 eV] of non-crystalline solids. The spectral features at an energy loss at ~ 100 -120 eV are due to the Si L -edge (corresponding to electron excitation from Si $2p$ to unbound state) XRS spectra for the glass (background due to Compton scattering is not subtracted here) (Fig. 2B). Figure 2C shows O K -edge XRS spectrum for the CaSiO_3 glass where typical and broad O K -edge features for oxide glasses at 538-540 eV are presented: the O K -edge feature is due to an excitation of a core electron from the oxygen $1s$ -state into unoccupied oxygen $2p$ -states that are hybridized with the silicon $3s$ - and $3p$ -states of four-coordinated Si atoms in corner-sharing SiO_4 (see section “Remaining Challenges and Outlook: Applications of New K -, L -, M -edge XRS, XRS with Momentum Transfer, In Situ High Temperature and Pressure XRS Study for Multi-Components Glasses” for further details of O K -edge XRS spectra for oxide glasses). Note that these multi-element and multiple-edge XRS spectra were collected without need of a vacuum chamber that is necessary for soft-x ray XAS studies of low- z elements. As previously mentioned, while the transition matrix in the XRS scattering cross section (Eqn. 6) is identical to that of XAS, multipole transitions can be probed by exploring the momentum transfer (when qr becomes larger). The q dependence on XRS spectra for diverse materials has been explored in order to study the nature of the bonding processes in such phenomena as the indirect band gap of dielectrics, the nature of excitons, and orbital symmetry (Caliebe et al. 2000; Hamalainen et al. 2002; Soininen et al. 2006) (see Schulke 2007 and references therein).

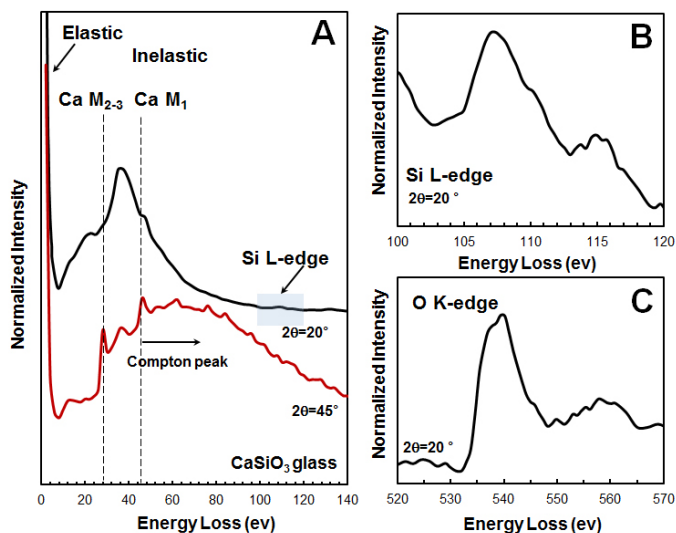


Figure 2. XRS spectra for CaSiO_3 glass with varying scattering angle (2θ) as labeled. The spectrum is plotted as normalized scattered intensity versus energy loss (incident energy – elastic energy). Elastic energy is 9.694 keV. (A) Ca $M_{2,3}$, Ca M_1 edges, Si L -edge X-ray Raman scattering (XRS) spectra and Compton scattering peak for CaSiO_3 glass. (B) Si L -edge XRS spectra for CaSiO_3 glass at scattering angle of 20° . (C) O K -edge XRS spectra for CaSiO_3 glass at scattering angle of 20° .

Comparison with other high pressure probes of structure of non-crystalline oxides. XRS compliments other established spectroscopic and scattering techniques that give unique data on the structure of materials under compression. As we provide extensive discussion on the application of XRS techniques to explore the structure and bonding nature of glasses or non-crystalline solids, here we briefly mention the advantages of XRS techniques over other high-pressure probes of glass structure.

Elastic X-ray scattering techniques provide essential information of the electron density of materials (and its structure factor) and average lattice structure, making it mostly suitable for studying crystalline materials under compression. Applications of synchrotron elastic X-ray scattering to low- z glass, including oxide glasses (silicates, borates) at high pressure has been limited due to the highly attenuating sample environment and small atomic scattering factors of low- z elements (e.g., oxygen, silicon, boron). While neutron scattering experiments for low- z glasses can overcome this problem and are potentially promising, they require relatively large sample volumes, which limits the current pressure range of study to below 10-20 GPa (e.g., Salmon et al. 2013). Additionally, with an increasing number of components, the overlap among structure factors or pair-correlation functions from both elastic X-ray and neutron scattering becomes problematic. The detailed pair correlation functions for cation-anion (or cation-cation, anion-anion) pairs are thus difficult to obtain as the number of components in oxide glasses increases.

Vibrational spectroscopy (such as Raman and IR) has been effective in providing vibrational density of states of materials (mostly for crystalline and molecules) at high pressure and can be performed *in situ*. The spectra for amorphous oxides are often quite broad even at 1 atm and due to an increase in topological disorder with pressure, the modes (or peaks) gets even further broadened, often yielding ambiguous results at high pressure.

This trend in an increase in overlap among modes or structure factors is inherent in any experimental measurement for amorphous materials under compression. This problem can be partly resolved using element-specific experimental probes, such as XRS and multi-nuclear solid-state nuclear magnetic resonance (NMR). Previous solid-state NMR studies of oxide glasses have provided improved resolution among the detailed atomic structures in the glasses and thus their pressure-induced structural changes (see Allwardt et al. 2005a,b; Kelsey et al. 2009a,b; Lee 2010, 2011). For example, it has been shown that the pressure-induced structural changes are characterized by the formation of bridging oxygen (BO) linking ^{14}Si and highly coordinated Si and Al at the expense of nonbridging oxygen (NBO) at high pressure (Xue et al. 1994; Yarger et al. 1995; Lee 2010, 2011). However, solid-state NMR studies require 10-20 mg samples, limiting the maximum quench pressure for oxide glasses to 10-12 GPa (Xue et al. 1989; Yarger et al. 1995; Lee et al. 2003; Allwardt et al. 2004). Therefore the structure of glasses for the NMR experiments represents that of super-cooled liquids at the glass transition temperature, below which the melt structures are frozen at high pressure. *In situ* high-pressure NMR spectroscopy of solids is currently not possible. The inherent difficulties of the current technologies pose major challenges for probing structural changes of low- z glasses over a wide pressure ranges. The XRS technique can resolve most of the aforementioned problems of conventional experimental probes, as well as yield a new opportunity to study the bonding changes in low- z systems at high pressure.

Current limitations of XRS technique. We also note that there are several disadvantages of XRS spectroscopy. Because XRS utilizes inelastically scattered X-ray photons, the intensity of the X-ray Raman signal is several orders of magnitude smaller than that of an elastic X-ray signal. The XRS process is thus intrinsically inefficient, requiring relatively long collection times to provide statistically meaningful experimental results with sufficient signal/background ratios: as for the spectra presented in the current review, collection time varies from several hours to \sim a day depending on the atoms of interest, as well as, the type and dimension of the

sample (see below for further details). The stability (and drift) of the synchrotron X-ray beam should thus be regularly checked during collection of the XRS signal. Furthermore, XRS has only been applied to a limited number of elements from He up to Na *K*-edge. This is largely because the X-ray Raman signal intensity decreases with atomic number.

Practical glitches involving XRS experiments under static compression. XRS studies involving low-*z* elements enable us to unveil structural details of densification in oxide glasses at pressures up to ~ 50 GPa. Application of XRS to oxide glasses synthesized at higher pressure above 50-70 GPa remains to be explored. This has been limited due mostly to the following experimental technical difficulties. First, as the gap between diamond anvils decreases with increasing pressure, unless a beam size of a few μm with significantly improved photon flux could be used, it is difficult to get sufficient *q*-ranges for the IXS experiment with radial X-ray radiation through the Be gasket. Taking into consideration the ranges of pressure in the Earth's and planetary interiors (up to 360 GPa to the Earth's inner core) and variations in composition in the diverse earth and planetary materials, a considerable amounts of future studies spanning much higher pressure conditions are necessary. Additionally, as previously mentioned, X-ray attenuation depth of the many oxides (including iron oxides) is rather small (~ 10 μm for 10 keV X-rays). The limited sample volume due to small X-ray attenuation length makes it difficult to get sufficient signal from the sample at high pressure: sample volume of oxides interacting with incident X-rays can decrease significantly because of the small X-ray attenuation length of many transition metal bearing crystalline and amorphous oxides. The combination of sample dimension for high pressure research and X-ray attenuation lengths needs to be taken into consideration to optimize sample size for XRS with a DAC. Third, the pressure gradient in the DAC increases with increasing pressure. Depending on the size (FWHM) of the X-ray beam, the IXS signals from a sample with varying pressure range (instead of a single pressure condition) can be collected with a typical size of 60 μm (H) \times 20 μm (V). It should also be mentioned that with the possible exceptions of B and C *K*-edge XRS studies, currently it takes ~day(s) of beamtime to achieve a signal to noise (and/or background) ratio in the oxygen and other *K*- and *L*- edge XRS spectra under typical experimental conditions for the current XRS beam lines with ~ 1 eV resolution. This makes it difficult to check reproducibility of the experimental results. New cell design with enhanced X-ray flux and reduced beam size would thus be necessary. Better X-ray optics with focusing and enhancing signals from a few μm beam are being developed for XRS techniques and will be eventually overcome the aforementioned limitations.

XRS experiments

Hard X-rays at 3rd generation synchrotron radiation sources with flux densities of approximately 10^{13} - 10^{14} photons/s/eV are used to collect XRS spectra. While most of the experimental XRS data shown here were obtained from sector 16 ID-D (HPCAT) and 13-IDC (GSECARS) at the Advanced Photon Source (APS), NRIXS spectra can be collected at other 3rd generational synchrotron radiation facilities including SPring-8 (BL12-XU), and the European Synchrotron Radiation Facility (ESRF) (e.g., Bergmann et al. 2002a; Fister et al. 2006, 2007; Lelong et al. 2012).

The experimental conditions for XRS studies at high pressure using a DAC have been reported previously (Mao et al. 2003; Schulke 2007; Rueff and Shukla 2010). The detailed information of instrumentation and X-ray optics can be found in recent manuscripts (Bergmann et al. 2002a; Fister et al. 2006, 2007). Current progress and review of DAC techniques can also be found elsewhere (Mao and Mao 2007; Shen and Wang 2014, this volume). In the typical XRS experiment, samples are loaded into the sample chamber of a gasket (typically made from Be or BN) in a DAC with a few ruby spheres as the pressure calibrant (Mao and Mao 2007). A pressure medium is not often used in the typical XRS study for materials at high pressure. This is in order to minimize scattering and/or absorption from the medium. The stress condition

in the DAC is therefore uniaxial without the pressure medium, although the orientation effect in glass is less important than in the crystals. Future experiments with hydrostatic conditions (with the pressure medium) are certainly necessary to explore the effect of stress conditions on the pressure-induced changes in electronic bonding environment. Diamonds with varying flat culets have been used for high-pressure X-ray Raman experiments up to 74 GPa (Fukui et al. 2008).

XRS spectra are collected by scanning the energy of the incident beam relative to the analyzer with a fixed elastic energy (E_0) that varies depending on analyzer setting (e.g., 9.886 keV at the BL12XU, 9.692 at the GSECARS, and 9.686 keV at the HPCAT). A linear array of multiple spherical Si(660) analyzers operating in a backscattering geometry were used for the study at the APS and an array of multiple Si(555) analyzers are used for experiments performed at BL12-XU (see Lee 2008 and references therein). The backscattered X-rays are focused into a single detector with the typical instrument energy resolution of 1.0 eV. While the resolution can be further enhanced (\sim meV) for verification of detailed edge features (or probing of phonon dynamics of solids) (e.g., by implementing spectrometer optics utilizing the higher-order asymmetric Bragg back scattering optics; Shvyd'ko et al. 2006; Stetsko et al. 2011), the \sim 1 eV resolution is adequate for revealing many major K -edge features in the XRS spectra for crystalline and amorphous oxides and their shifts as a function of pressure and momentum transfer.

The X-ray Raman scattering signals are collected at varying scattering angles, but typically \sim 15-30° for high pressure experiments. The X-ray beam size (FWHM) varies but is typically \sim 60 μm (W) \times 20 μm (H) at the GSECARS and HPCAT and 20 μm (W) \times 20 μm (H) at the BL12-XU. Raw XRS spectra are background-subtracted, and most spectra are normalized to the continuum energy tail (see section “*Pressure-Induced Structural Changes in Crystalline and Amorphous Earth Materials: Insights from X-Ray Raman Scattering*” below). In addition, by comparing the spectra from different beam lines, the uncertainty in the edge energy of the spectra can be identified and is usually less than 0.4 eV: this aspect has been discussed in the recent manuscript (Lee et al. 2008b, supplementary information). The pressure uncertainties and the pressure gradient across the sample can be obtained from multiple measurements from the ruby spheres before and after the X-ray measurements.

PRESSURE-INDUCED STRUCTURAL CHANGES IN CRYSTALLINE AND AMORPHOUS EARTH MATERIALS: INSIGHTS FROM X-RAY RAMAN SCATTERING

Recent experimental results utilizing multi-edge, multi-element XRS spectroscopy are summarized in this section. We first present previous XRS studies involving the boron K -edge (\sim 190 eV), carbon K -edge (\sim 280 eV), and oxygen K -edge (\sim 530 eV), which are often suitable for XRS measurements at high pressure (yielding moderate quality of signal/background ratios with \sim 100-300 μm X-ray attenuation length, depending on sample density). These prominent element edges are thus relatively well-understood. We then provide an overview of previous XRS studies involving other lesser known or/and poorly studied edges (and thus more difficult to probe), such as helium K -edge (\sim 23 eV), lithium K -edge (\sim 60 eV), and nitrogen K -edge (\sim 410 eV). We also briefly mention the previous (and the new) XRS studies involving L and M -edges of Ca and Si in glasses. We have not attempted to provide an extensive review of all the experimental results using IXS as excellent accounts of these diverse IXS measurements of materials under compression can also be found in the reviews of Rueff and Shukla (2010) and Schulke (2007).

Application of *K*-edge XRS to materials under high pressure

Boron *K*-edge XRS study of earth materials under compression. Boron *K*-edge XRS (as well as XANES) has been one of the most effective probes for B coordination environments (^{13}B , and ^{14}B) because these two distinct B coordination environments are relatively well-distinguished in the XRS spectrum: as for boron containing phases at 1 atm, previous XAS studies showed that these ^{13}B (characterized with π^* bonding at ~ 194 eV), and ^{14}B (with features at ~ 197 -200 eV) environments are well-resolved (see Fleet and Muthupari 1999, 2000 and references therein). XRS has been utilized to explore the structural details (direct and quantitative measurements of B coordination transition) of crystalline boron nitride and archetypal amorphous borates and alkali borate glasses with varying pressure up to ~ 30 GPa.

Pressure-induced bonding transitions in crystalline boron nitride (BN). BN was one of the first crystals explored using XRS at high pressure. Hexagonal boron nitride (*h*-BN) and hard cubic phase (*c*-BN) have diverse technological applications (Meng et al. 2004). Boron *K*-edge XRS spectroscopy revealed pressure-induced bonding transitions of boron and nitrogen in *h*-BN to a hexagonal close-packed wurtzite type structure (*w*-BN). The sp^2 - and p -bonding in *h*-BN is transformed into sp^3 -bonding stemming from the formation of a three-dimensional tetrahedron framework in *w*-BN (Meng et al. 2004). Figure 3 shows boron (B) *K*-edge XRS spectra for BN with varying pressure. The XRS spectra at 1 atm show the π and σ bonds characteristics of *h*-BN (as labeled). Pressure-induced changes in intensities of π^* and σ^* bonds (indicating the presence of π and σ bonds) were apparent. These changes show an orientation dependence, leading to the preferred orientation of *h*-BN where its *c* axis is parallel to the DAC axis. After further increase in pressure up to 14 GPa, the *w*-BN phase was formed as indicated

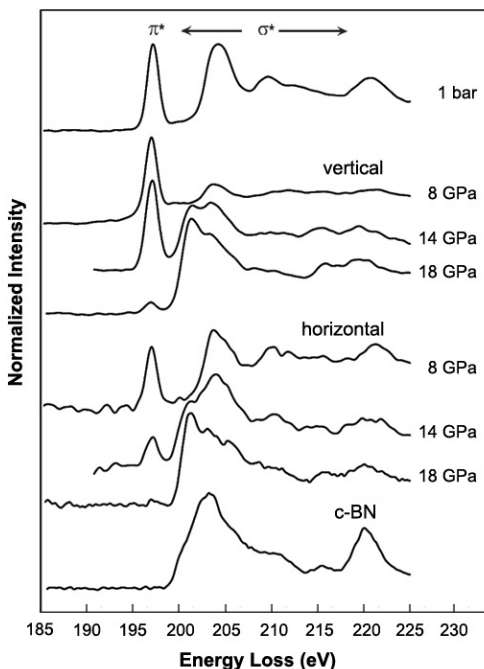


Figure 3. Boron *K*-edge XRS spectra of BN with varying pressure. The spectra are plotted as normalized scattered intensity versus energy loss (incident energy – elastic energy). The spectra were collected in both vertical and horizontal geometries to probe bonds in directions parallel and perpendicular to the *c* axis of BN (modified from Meng et al. 2004).

by the appearance of the new feature at ~ 196 eV in the B K -edge XRS spectrum. While the XRS features for w -BN and c -BN are rather similar, their relative intensities of XRS features (in the range from 194 to 200 eV and at 215 eV) are slightly distinct, indicating the difference in the distribution of electronic densities of state for each phase (Meng et al. 2004).

Pressure-induced changes in boron coordination environments in pure borate (B_2O_3) glasses at high pressure.

While the structure of borate glasses at 1 atm is relatively well known mainly from ^{11}B NMR (see Eckert 1992 and the references therein), pressure-induced changes in coordination for low- z glasses, including borates, remain unsolved in modern physical chemistry, condensed matter physics, glass sciences, and earth science due to the lack of suitable experimental probes. Pure borate glasses have fundamental importance as prototypical glass formers (along with silica). Pressure-induced coordination transformation of the B cations can provide insights into structural evolution of multi-component covalent oxide glasses with pressure (Wolf and McMillan 1995; Yarger et al. 1995; Poe et al. 1997).

Figure 4 (top) shows the boron K -edge XRS spectra for B_2O_3 and $Na_2B_4O_7$ glasses at 1 atm: Note that at 1 atm all boron atoms in the B_2O_3 glass are $^{[3]}B$ and $Na_2B_4O_7$ glass consists of $\sim 45\%$ of $^{[4]}B$ and thus we show the XRS spectrum for $Na_2B_4O_7$ glass to show the spectral features for $^{[4]}B$. The feature at 194 eV corresponds to the transition of a core boron $1s$ electron to an unoccupied boron antibonding $2p_z$ orbital (labeled π^*) and is due to three-coordinated boron ($^{[3]}B$) in the glasses. The broader features centered at ~ 203 eV corresponds predominantly to a transition from a B $1s$ to unoccupied B-O σ^* antibonding orbital (labeled σ^*) and is also associated with $^{[3]}B$ (Schwarz et al. 1983). The XRS spectrum for $Na_2B_4O_7$ glass (with $\sim 45\%$ of $^{[4]}B$) show another σ^* feature around at 198-200 eV that corresponds to a $1s$ to $2p/2s$ σ^* antibonding orbital transition in four-coordinated boron ($^{[4]}B$) (Fleet and Muthupari 1999, 2000). The decrease in π^* intensity for $Na_2B_4O_7$ glass (compared with that of B_2O_3 glass) indicates an increase in

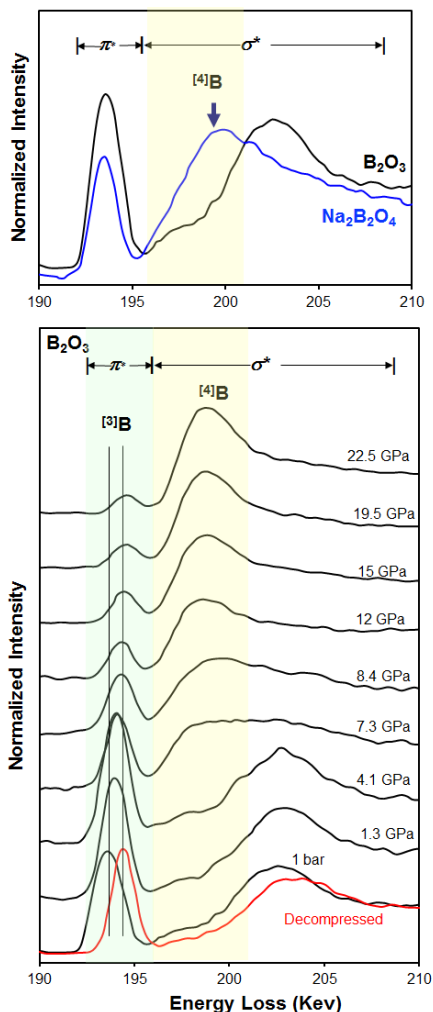


Figure 4. (top) Boron K -edge XRS spectra for B_2O_3 (black) and $Na_2B_4O_7$ (blue) glass at 1 atm [plotted as Normalized scattered intensity vs. Energy loss (incident energy – elastic energy of 9.692 keV)] (modified from Lee et al. 2005). (bottom) Boron K -edge XRS spectra for B_2O_3 glass at pressures ranging from 1 bar to 22.5 GPa. Some pressure uncertainty exists due to the slow equilibration of ν - B_2O_3 after each pressure change. The experiment was repeated with different DACs and observed similar pressure response was observed, suggesting that this behavior is intrinsic to the sample, as reported previously (modified from Lee et al. 2005).

⁴¹B bonds and is consistent with NMR measurements and XANES study of ν -B₂O₃ (Fleet and Muthupari 1999, 2000).

Figure 4 (bottom) shows boron *K*-edge XRS spectra for B₂O₃ glass under varying pressures (Lee 2005). XRS spectra show negligible changes at pressures up to ~4.1 GPa. At 7.3 GPa, π^* intensity (due to ¹¹B) drops drastically and the σ^* component due to ¹⁰B (~198-200 eV) increases. With a further increase in pressure up to 22.5 GPa, most of the ¹¹B is transformed into the ¹⁰B. While the coordination transformation is reversible, the energy shift of the π^* peak remains upon decompression, implying permanent densification associated with boron topology due to a decrease in boroxol ring fraction (tri-membered planar borate ring) (see Lee 2005, 2010 and references therein). The XRS results for B₂O₃ glass provided the first ‘*in situ*’ and unambiguous experimental evidence of a reversible coordination transformation along with an irreversible topological densification in borate glasses.

Pressure-induced changes in boron coordination environments in alkali borate glasses at high pressure: implications for densification mechanisms of oxide glasses. The cation field strength (i.e., charge/ionic radii) of network-modifying cations (e.g., Li⁺, Na⁺) affects the thermodynamic properties and viscosity of silicates melts at both ambient and high pressure (e.g., Navrotsky 1995). The effect of cation field strength on the densification in oxide glasses has been recently explored using the XRS technique. The XRS results revealed the marked difference in densification behavior in borate glasses with varying cation field strength: B *K*-edge XRS spectra for borate and alkali borate glasses (Li₂B₄O₇ and Na₂B₄O₇) were probed at high pressure up to 30 GPa with an aim to provide pressure-induced coordination transformation from ¹¹B to ¹⁰B (Lee et al. 2007, 2008a). Figure 5A presents the B *K*-edge XRS spectra for Li₂B₄O₇ glasses with varying pressures up to 30 GPa. With increasing pressure, the σ^* (¹⁰B) feature near 198–200 eV increases while π^* intensity (¹¹B) gradually decreases. Figure 5B present the XRS spectra of Na₂B₄O₇ glasses with varying pressure. A π^* feature at approximately 194 eV (¹¹B) decreases while the σ^* feature associated with ¹⁰B increases, consistent with the trends reported for pure borate and Li-borate glasses (Lee et al. 2005, 2007).

Quantification of boron coordination environments. The quantitative fractions of boron coordination states provide information necessary to establish effect of pressure on the bonding transitions. As the quantification of the spectra can be of practical importance, the procedure of yielding quantitative ¹¹B fraction is given below (Fig. 6): the raw XRS spectra were background-subtracted and then were normalized to the continuum energy tail above approximately 210 eV, leading to spectra with a plateau above approximately 205 eV (Fig. 6, blue spectrum). Then, linear backgrounds extending from a π^* peak (around 193-194 eV) to 210 eV were subtracted as suggested by previous B *K*-edge XANES studies (e.g., Fleet and Muthupari 1999, 2000) to obtain quantitative fraction of boron coordination environments. Figure 6 presents the XRS spectra before and after linear background subtraction for the quantification of $X(^{11}\text{B}_{\text{sample}})$ in the borate glasses studied here. The total intensity of the spectra [$J(\text{total})$] from 192 eV to 210 eV was subsequently obtained. Then, the spectral intensity for π^* feature [$J(\pi^*)$] was obtained by fitting it with a single Gaussian function. The ratio between [$J(\pi^*)$] and [$J(\text{total})$] was then calculated [i.e., $J(\pi^*)/J(\text{total})$]. The ratio was further normalized to the ratio of spectral intensity in the B *K*-edge of reference material with 100% ¹¹B, i.e., pure B₂O₃ glass at 1 atm [$J(\pi^*)/J(\text{total})$]_{pure B₂O₃ glass}. Its estimated value is 0.354, which is in excellent agreement with the average value predicted from the borate crystals with only ¹¹B (0.354, Garvie et al. 1995). The mole fraction of ¹¹B in sample borate glass [$X(^{11}\text{B})$] is thus calculated from the following relation:

$$X(^{11}\text{B}_{\text{sample}}) = \frac{[J(\pi^*)/J(\text{total})]_{\text{sample}}}{[J(\pi^*)/J(\text{total})]_{\text{pure B}_2\text{O}_3 \text{ glass}}} \quad (7)$$

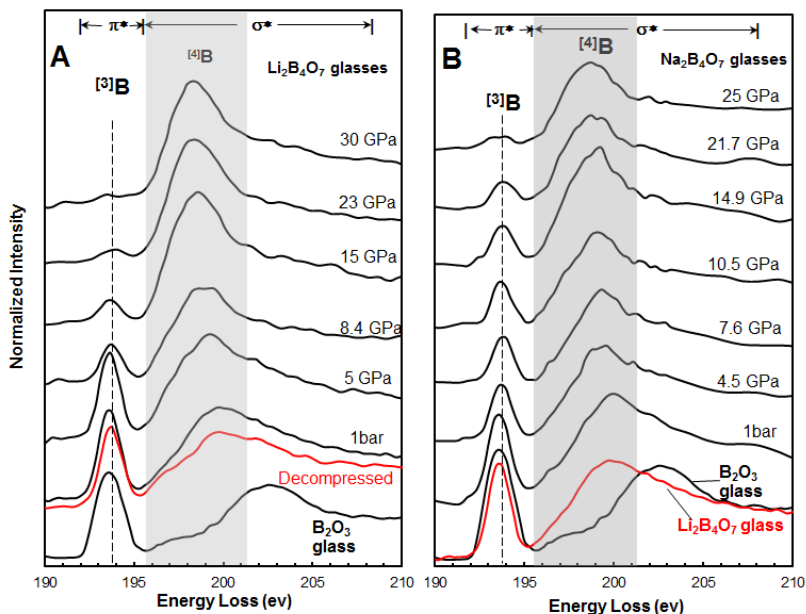


Figure 5. (A) Boron K -edge XRS spectra for $\text{Li}_2\text{B}_4\text{O}_7$ glass and B_2O_3 glass (bottom) at pressures ranging from 1 bar to 30 GPa as labeled. Thin line refers to XRS spectra for $\text{Li}_2\text{B}_4\text{O}_7$ glass decompressed to 1 atm from 30 GPa. The spectra are plotted as normalized scattered intensity vs. energy loss (incident energy – elastic energy (9.687 keV)) (Modified from Lee et al. 2007). The inelastic X-rays were collected with a linear array of six spherical Si(660) analyzers operating in a backscattering geometry, and at an angle of 30° (for ambient condition) and 18° (for high-pressure experiment) off the incident beam direction. The monochromatic X-rays produced by a cryogenically cooled double crystal Si(111) monochromator were focused to $20 \times 20 \mu\text{m}$ ($H \times V$) with a large KB mirror pair. While previous studies of B_2O_3 glasses high pressure reported that pressure response of cold pressed glass appeared to be slow, necessitating the equilibration time of about several hours (Wright et al. 2000; Lee et al. 2005), this slow pressure equilibration was not observed for Li-borate glasses. (B) Boron K -edge X-ray Raman scattering spectra of Na-diborate ($\text{Na}_2\text{B}_4\text{O}_7$) glasses with varying pressure, as labeled. The spectra are plotted as the normalized scattered intensity vs. the energy loss (incident energy – elastic energy) (modified from Lee et al. 2008).

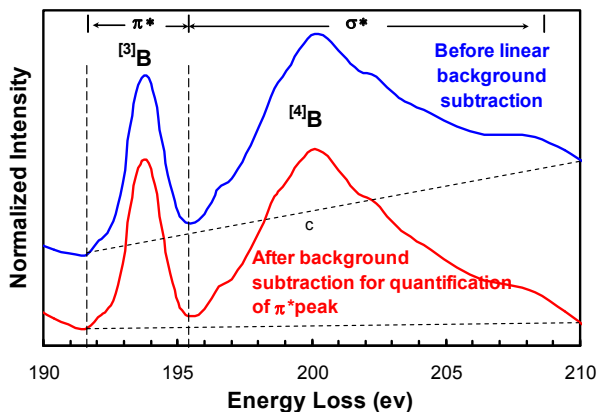


Figure 6. Quantification of boron K -edge XRS spectrum for Na-diborate ($\text{Na}_2\text{B}_4\text{O}_7$) glass at 1 atm (blue spectrum). Linear background subtracted spectrum for the Na-borate glasses for quantification of π^* was also shown (red spectrum).

The robustness of the above method has been tested in previous studies (e.g., Garvie et al. 1993; Sauer et al. 1993), although it could somewhat overestimate ^{13}B at low concentrations and may underestimate it at high concentrations. Furthermore, the ^{13}B fractions in Na- and Li-diborate glasses at 1 atm (approximately 50%) are rather consistent with predicted fraction from B-11 NMR (about 55%). Whereas slightly better agreement (3-4 % deviation from NMR) can be reached by extending the spectral range above 210 eV as suggested by the earlier quantification of ^{13}B fraction in borosilicate glasses for larger $\text{Na}_2\text{O}/\text{B}_2\text{O}_3$ ratio (> 1) (Fleet and Muthupari 1999), the $[J(\pi^*)/J(\text{total})]_{\text{pure B}_2\text{O}_3 \text{ glass}}$ decreases with extension of spectral range and it further deviates from 0.354. This suggests that the spectral intensity up to 210 eV is reasonable approximation for the quantification of ^{13}B fraction ($X^{13}\text{B}$). We note that upon calibration of ^{13}B fraction based on the above procedure, ^{14}B fraction ($X^{14}\text{B}$) is simultaneously calibrated as a function of concentration and pressure because of constraints in the mole fractions of these two species (i.e., $X^{14}\text{B} = 1 - X^{13}\text{B}$). Uncertainty in the current method may result from the absence of a high pressure borate standard with known ^{13}B fraction.

Figure 7 shows the variation in the ^{13}B fraction in alkali borate glasses with pressure (Lee et al. 2007, 2008a). The pressure-induced boron coordination transformation from ^{13}B to ^{14}B in Na-diborate glass (blue line) is *linear* with pressure: ^{13}B proportion in Na-borate glasses (blue line) decreases with pressure from $\sim 47 \pm 4\%$ (at 1 atm) to $16\% \pm 4\%$ at 25 GPa. The results for Li-borate glasses (red line) show a *nonlinear* coordination transformation with *multiple* $(\partial^{13}\text{B}/\partial P)_T$. Pure borate and Li-borate glasses show three distinct regions of $(\partial^{13}\text{B}/\partial P)_T$ values: in low-pressure ranges (I) $(\partial^{14}\text{B}/\partial P)_T$ is the smallest. In the intermediate-pressure range (II) a dramatic coordination changes (and thus largest $(\partial^{14}\text{B}/\partial P)_T$) are observed. With further increases in pressure [range (III)], a considerably smaller $(\partial^{14}\text{B}/\partial P)_T$ were observed (Lee et al. 2007, 2008a). The observed trends demonstrate the effect of cation field strength (in particular, ionic radii) on the densification behavior of borates (Lee et al. 2008a). While the small ionic radii of Li^+ (0.76 Å) may not alter the densification mechanisms observed for pure borate glasses, the larger ionic radii of Na^+ (1.02 Å) in borates significantly affect the structural transition with pressure. $(\partial^{14}\text{B}/\partial P)_T$ may be regarded as the measure of an energy barrier for the boron coordination transformation. On the basis of this premise, pure and Li-borate glasses have at least three distinct energy barriers for coordination transformation and thus multiple densification mechanisms. For Na-borate glasses, the change is more gradual with a single transformation energy barrier for boron coordination transformation (Lee et al. 2008a).

A conceptual model was introduced to account for the observed trends, utilizing pressure flexibility (the resistance to structural changes with increased pressurization) defined by the variance of the ratio of energy difference between high and low pressure states to its pressure gradient (see Lee et al. 2008a and references therein). It should also

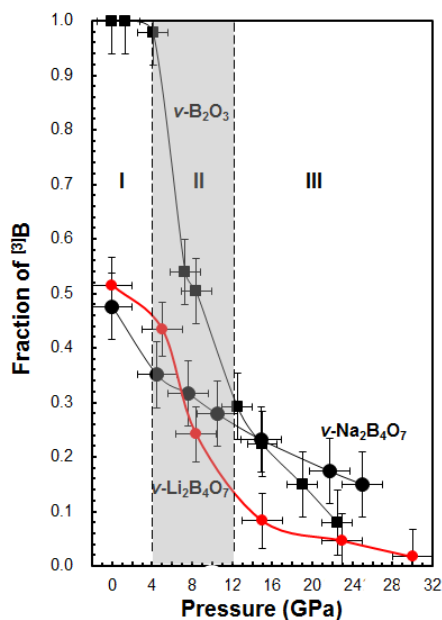


Figure 7. Pressure dependence of the ^{13}B fraction for $\text{Na}_2\text{B}_4\text{O}_7$ glass and $\text{Li}_2\text{B}_4\text{O}_7$ glass. The black dashed lines for I, II, and III represent distinct pressure ranges with varying $(\partial^{14}\text{B}/\partial P)_T$ values (modified from Lee et al. 2008).

be mentioned that before the first application of X-ray Raman scattering technique, little was known about the structure of borate glasses at high pressure. However, the progress in these techniques make borate glasses one of only a few model oxide glasses in which detailed densification mechanisms have been established (Lee et al. 2008a). We believe that the aforementioned model can be applied to diverse glass forming liquids with varying degree of fragility.

Oxygen K-edge XRS studies of earth materials under pressure. The O K-edge XRS (and thus XAS) features of oxides provide the electronic structure around oxygen from the information of the unoccupied oxygen 2*p*-state, and thus detailed oxygen coordination environments (de Groot 2001). Previous O-K edge XANES studies have shown that the O K-edge features (~0.5-1 eV) depend on local structures and chemical compositions, and overall topology of cations around the oxygen (e.g., Si-O and O-O bond lengths, oxygen coordination environments, and Si-O-Si bond angles) (Ching and Rulis 2008 and references therein). The previous studies have also shown that the O K-edge is useful for probing the pressure-induced changes in local electronic structures in crystalline oxides at high pressure (Lee et al. 2008b). For example, oxygen K-edge X-ray Raman spectra for SiO₂ and MgSiO₃ polymorphs and amorphous phases show characteristic K-edge features stemming from their local atomic configurations (corner sharing, edge-sharing, and Si coordination number) and topology (bond angle and length) around oxygen (Lin 2007; Lee et al. 2008b; Fukui et al. 2009a; Yi and Lee 2012).

Oxygen K-edge XRS has also been applied to the study of fluids and non-crystalline materials, revealing the pressure-induced changes in the electron bonding transitions in glasses (SiO₂, B₂O₃, GeO₂, MgSiO₃), H₂O, and O₂ phases at high pressures (Wernet et al. 2004; Lee et al. 2008b; Meng et al. 2008; Fister et al. 2009). In particular, revealing the bonding nature of H₂O polymorphs with varying pressure and temperature conditions is essential to understand their characteristic properties. Earlier XRS studies of water and related phases with varying pressure, first unveiled the utility, as well as, the capability of the technique by probing the intermediate-range structure of liquid water (Wernet et al. 2004). Additionally, O K-edge XRS experiments for ice phases have revealed characteristic O K-edge features due to their distinctive local configurations (Bergmann et al. 2002a; Cai et al. 2005; Meng et al. 2008; Fister et al. 2009): the features are also dependent on the proton positions as well as oxygen topologies. As a review of previous O K-edge XRS study of H₂O polymorphs can be found elsewhere (e.g., Fister et al. 2009), these phases will not be discussed here. Other phases are discussed in the following section. Additionally, the X-ray induced dissociation of H₂O phase under pressure is briefly mentioned (Mao et al. 2006).

Pressure-induced electron bonding transitions in dense oxygen. O K-edge XRS studies of O₂ polymorphs at high pressure showed the pressure-induced bonding mechanisms in the dense fluid (i.e., intermolecular bonding) and molecular solids (i.e., intercluster bonding) (Meng et al. 2008). Figure 8 presents O K-edge XRS spectra for oxygen in dense fluid and solid β -, δ -, and ϵ -phases up to 38 GPa at room temperature. The peak position of gas-phase O₂ is schematically illustrated (a π^* peak at 530.8 eV and two weak

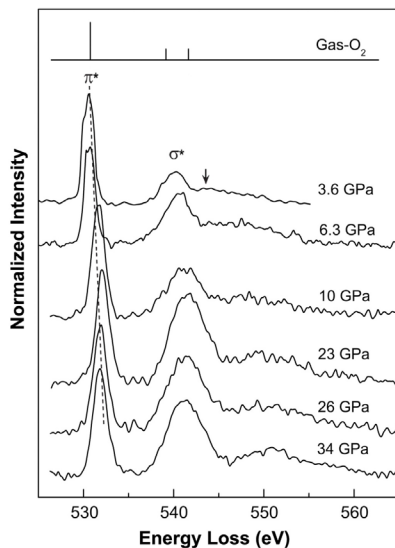


Figure 8. Oxygen K-edge XRS spectra for oxygen in dense fluid and solid β -, δ -, and ϵ -phases up to 38 GPa at room temperature (modified from Meng et al. 2009).

σ_u^* peaks at 539.2 eV and 541.7 eV). Additionally, the intensity of the second σ^* feature of fluid- O_2 at 3.6 GPa is smaller than those of the gas phase. The peak width of the second peak (arrow) is also broadened upon pressurization, indicating a broadening of the Rydberg states in the condensed fluid phase. The XRS spectra for high-pressure oxygen phases show similar spectral features (π^* and σ^*). Below 10 GPa, the σ^* edge peak position of the dense fluid phase gradually moves to higher energy while the π^* peak energy remains constant up to 10 GPa. Upon transition to the ε -phase at 10 GPa, a ~ 1 eV shift in the π^* peak is observed. With further increase in pressure from 10 to 38 GPa, both π^* and σ^* transition energies show slight but gradual increases (and then decrease) with pressure. The relative intensity of the π^* feature decreases with pressure for low pressure phases while it does not change much for the ε -phase (see Meng et al. 2008 for further discussion). At low pressure, below 10 GPa, the results indicate that densification of O_2 molecules enhances intermolecular interactions, leading to π orbital delocalization. The ε -phase consists of $(O_2)_4$ clusters and an increase in interactions between $(O_2)_4$ clusters in the ε -phase leads to stronger intercluster bonding with increasing pressure (Meng et al. 2008).

X-ray-induced dissociation of H_2O and formation of an O_2 - H_2 alloy at high pressure. The XRS technique requires long exposure to moderately high energy (~ 10 -keV) X-ray radiation (up to several days). X-ray radiation of a sample at high pressure, if the absorption conditions are met, can often induce the dissociation of molecules. Recent O K -edge XRS spectra of H_2O have revealed the X-ray radiation- and pressure-induced dissociation of H_2O polymorphs: ice VII was converted into a molecular alloy of O_2 and H_2 (Fig. 9) (Mao et al. 2006). The O K -edge XRS spectra for dense water below 0.9 GPa, ice VI between 1 and 2 GPa, and ice VII just above 2 GPa show characteristic peaks at ~ 540 eV. At higher pressures above 2.5 GPa, a sharp peak at 530 eV is observed. The peaks are due to O–O π^* bonding in O_2 molecule, indicating X-ray-induced dissociation of H_2O molecules. The peak intensity grew with increasing time of exposure to the incident X-ray beam of ~ 10 keV and the change is apparently irreversible. The authors pointed out that the X-ray-induced dissociation in ice VII was most effective with X-ray

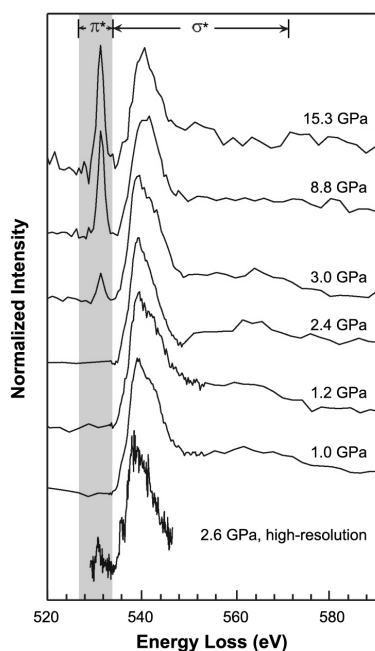


Figure 9. Oxygen K -edge XRS spectra of H_2O at high pressure after 12 hours of X-ray irradiation. The spectra are plotted as the normalized scattered intensity vs. the energy loss (incident energy–elastic energy). The bottom spectrum was collected at BL12XU, SPring-8 (9.886-keV X-ray radiation with high-energy resolution of 300 meV). The XRS spectra for H_2O collected at 1.0, 1.2, 2.4, 3.0, 8.8, and 15.3 GPa were collected with X-ray radiation elastic energy of 9.687 keV at beamline 13-IDC of the GSECARS, Advanced Photon Source with resolution of 1 eV (modified from Mao et al. 2006).

radiation energy of ~ 10 keV with a low absorbance Be gasket while at higher energy radiation (e.g., 30 keV) through the diamond anvil did not induce the dissociation (Mao et al. 2006).

Oxygen K-edge XRS study of archetypal oxide glasses (SiO_2 , GeO_2 , and B_2O_3) at high pressure. The oxygen configurations in amorphous oxides at high pressure can be directly probed using O *K*-edge XRS. The formation of highly coordinated framework cations (e.g., $^{[5,6]}\text{Si}$, $^{[5,6]}\text{Ge}$, $^{[4]}\text{B}$) in the fully polymerized prototypical single component oxide glasses such as SiO_2 , GeO_2 , and B_2O_3 glasses should be accompanied by the formation of the triply coordinated oxygen ($^{[3]}\text{O}$) (here we used the term “oxygen tricluster” for the triply coordinated oxygen as expected from the compositions, Lee et al. 2008b). Formation of oxygen triclusters has been suggested to be a dominant factor affecting the melt properties at ambient and high pressure (Angell et al. 1982; Diefenbacher et al. 1998; Stebbins and Xu 1997).

- **SiO_2 .** O *K*-edge XRS feature at 543 eV for SiO_2 glass at 39 GPa has been interpreted as the formation of stishovite-like $^{[6]}\text{Si}$ in SiO_2 glass at high pressures (Lin et al. 2007). The coordination transformation of Si in the fully polymerized SiO_2 glass is inevitably resulting in the formation of oxygen atoms that are triply coordinated by $^{[5,6]}\text{Si}$. The edge feature at 543 eV could thus result from the formation of the triply coordinated oxygen.
- **B_2O_3 .** The change in pressure-induced boron coordination also leads to a variation of oxygen environments with pressure (Lee et al. 2005). Figure 10 shows the oxygen *K*-edge XRS spectra for $\nu\text{-B}_2\text{O}_3$ at 1 atm and 8.4 GPa where a decrease in sharp features at 536 eV and an increase in σ^* (543 eV) with broadening of the feature were observed. This change is due to the fact that unpaired *p* orbitals in oxygen contribute to form $^{[4]}\text{B}$ by forming a σ bond with p_z in the $^{[3]}\text{B}$ with increasing pressure. Formation of $^{[4]}\text{B}$ at high pressure leads to decrease in the fraction of boroxol rings content and it is likely due to be accompanied by the formation of peculiar oxygen environment, with oxygen triply coordinated by three $^{[4]}\text{B}$ (Lee et al. 2005).
- **GeO_2 .** GeO_2 glass at high pressure has been recently studied with O *K*-edge XRS (current study and Lelong et al. 2012). While GeO_2 is isochemical to SiO_2 glass, the GeO_2 glass is more compressible (i.e., a larger compressibility) than SiO_2 glass and thus it show changes in short-range structure at much lower pressure ranges (see Micoulaut et al. 2006 and references therein). The previous XRS spectra exhibit characteristic pressure-induced changes in the O *K*-edge feature with double peaks (similar to that of rutile-type GeO_2 phase) (Lelong et al. 2012). On the basis of XRS studies of crystalline polymorphs with various Ge coordination states, the authors were able to obtain detailed Ge coordination environments ($^{[4,5,6]}\text{Ge}$) in GeO_2 glasses with pressure. Figure 11 shows the oxygen *K*-edge XRS spectra for GeO_2 glasses at 1 atm and 15 GPa. An increase in the σ^* region at ~ 544 eV is observed with pressure, consistent with those for SiO_2 glass under pressure at ~ 40 GPa. The fea-

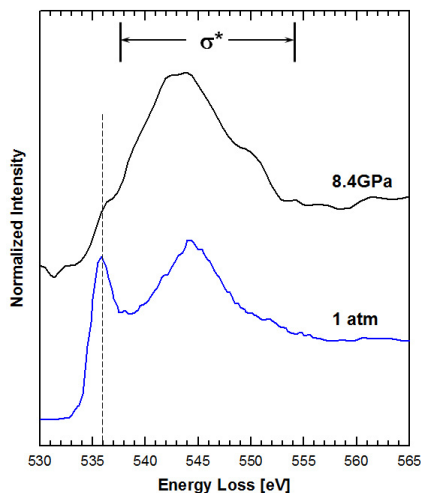


Figure 10. Oxygen *K*-edge XRS spectra for B_2O_3 glasses at 1 atm and 8.4 GPa. (Modified from Lee et al. 2004). The spectra are plotted as the normalized scattered intensity vs. the energy loss (incident energy–elastic energy).

ture could stem from the formation of highly coordinated Ge in the glasses and thus triply coordinated oxygen (which results from the formation of $^{[5,6]}\text{Ge}$).

Oxygen K-edge XRS study of crystalline MgSiO_3 polymorphs and MgSiO_3 glasses at high pressure. Crystalline and non-crystalline MgSiO_3 at high pressure have strong geophysical and geochemical implications for the mantle minerals and melts in earth and planetary interiors. Knowledge of the electronic and atomic structure of amorphous and crystalline MgSiO_3 polymorphs is essential to understand their elasticity, thermodynamic and transport properties in the mantle (e.g., Hemley 1998; Price 2007 and references therein). The potential presence of silicate melts at the top of the transition zone and in the core-mantle boundary has been suggested and it could have significant influences on the dynamics and properties of Earth's interior (Revenaugh and Sipkin 1994; Song et al. 2004; Caracas and Cohen 2006; Sakamaki et al. 2006; Agee 2008). MgSiO_3 -rich silicate melts were among the primary components of the early magma ocean. Despite essential roles of silicate melts in many geophysical and geochemical problems, little is known about the nature of bonding transitions in MgSiO_3 melts under the conditions of Earth's interior. O K-edge XRS studies of MgSiO_3 glass at high pressure up to 40 GPa suggested the formation of oxygen triclusters (oxygen coordinated with three Si frameworks; $^{[3]}\text{O}$) above 20 GPa in MgSiO_3 glass (Lee et al. 2008b).

Figure 12 shows the O K-edge spectra of MgSiO_3 glass with a dominant feature at 538–539 eV which show negligible changes in the pressure range between 1 atm and ~12 GPa (Lee et al. 2008b). Above 20 GPa, the spectra show a distinct feature at around 544–545 eV, wherein the spectral features gradually shift to higher energies with increasing pressure. The occurrence of the spectral feature near 545 eV at high pressures could arise from a variety of complex pressure-induced structural changes in the MgSiO_3 glass, such as the formation of the $^{[3]}\text{O}$ triclusters, an increase (or decrease) in the Mg–O distance, reduction in non-bridging oxygens, and formation of oxygen linking

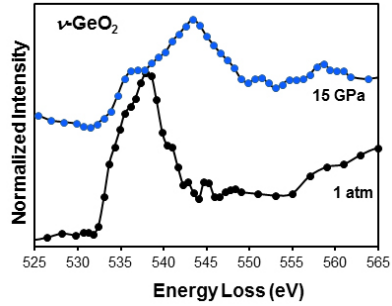


Figure 11. Oxygen K-edge XRS spectra for GeO_2 glasses at 1 atm and 15 GPa. The spectra are plotted as the normalized scattered intensity vs. the energy loss (incident energy – elastic energy).

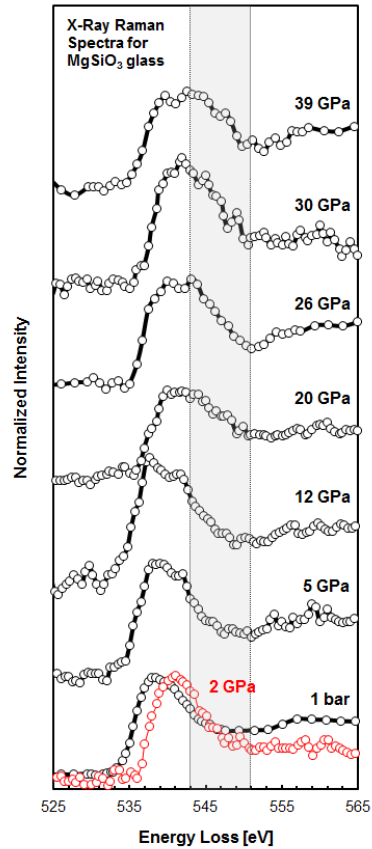


Figure 12. Oxygen K-edge XRS spectra for MgSiO_3 glasses at high pressures [plotted as normalized scattered intensity vs. energy loss (incident energy – elastic energy)]. Points refer to the step size of the energy scan of the experiments (modified from Lee et al. 2008).

^{44}Si and highly coordinated silicon such as $^{44}\text{Si-O-}^{56}\text{Si}$ and $^{60}\text{Si-O-}^{60}\text{Si}$. However, the exact atomistic origin for the feature is not clear (see section “*Insights from quantum chemical calculations*” below). Therefore, the authors studied the oxygen K -edge XRS for model crystalline MgSiO_3 and SiO_2 phases with known short-range local structures (Fig. 13). Detailed comparison of the O K -edge features for amorphous SiO_2 glass at 1 atm and MgSiO_3 glass, as well as polymorphs at high pressure, indicate that both NBO ($\text{Mg-O-}^{44}\text{Si}$) and BO ($^{44}\text{Si-O-}^{44}\text{Si}$) have similar oxygen K -edge features (Lee et al. 2008b). Although recent *ab initio* calculations of O K -edge features of crystalline chain silicates reported that bridging oxygen (BO) and nonbridging oxygen (NBO) in crystalline chain silicates show distinct oxygen K -edge features (Yi and Lee 2012) and see section “*Insights from quantum chemical calculations*” below for detailed analysis of an XRS spectrum with first principle calculations and references therein), a similar distinction was not observed in the oxygen K -edge spectra for the silicate glasses due to their inherent topological disorder (Lin et al. 2007; Lee et al. 2008b). The spectrum for ilmenite-type MgSiO_3 shows distinctive features at 537 and 541 eV. This peculiar feature for the edge-sharing oxygen configuration is similar to that of stishovite (Lin et al. 2007), indicating close proximity of oxygen with its second nearest neighbors. The oxygen K -edge spectrum of perovskite with all corner-sharing $^{60}\text{Si-O-}^{60}\text{Si}$ shows an increase in the intensity at approximately 543 eV, indicating pressure-induced Si coordination transformation. The feature in the quartz spectrum at around 546 eV apparently originates from its long-range periodicity (Davoli 1992).

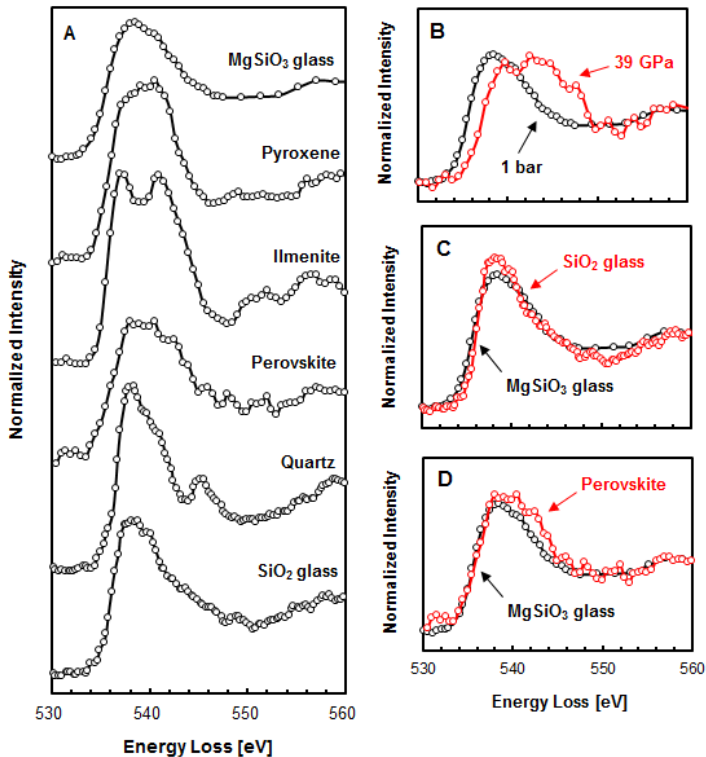


Figure 13. (A) Oxygen K -edge XRS spectra for crystalline and amorphous SiO_2 and MgSiO_3 at 1 atm and their high-pressure polymorphs. (B) Oxygen K -edge spectra for amorphous SiO_2 and MgSiO_3 at 1 atm. (C) Oxygen K -edge spectra for pyroxene (enstatite) and quartz. (D) Oxygen K -edge X-ray Raman scattering spectra for MgSiO_3 glass at 1 atm and perovskite (modified from Lee et al. 2008).

The significantly different oxygen coordination environments for perovskite and glass at 1 atm (i.e., $^{16}\text{Si-O-}^{16}\text{Si}$ for perovskite vs. $^{14}\text{Si-O-}^{14}\text{Si}$ and $\text{Mg-O-}^{14}\text{Si}$ for MgSiO_3 glass at 1 atm) cannot explain the significant changes observed for the glasses at high pressures (Lee et al. 2008b). However, as similar K -edge features at ~ 544 eV in fully polymerized glasses have been observed and indicated that the features are due to the formation of oxygen tricluster associated with the formation of highly coordinated Si (see section “XRS experiments”), the oxygen K -edge feature at ~ 544 eV in the MgSiO_3 glass at pressures above 20 GPa may be attributed to the formation of the triply coordinated oxygen and changes in the short- to medium-range structures that are associated with the formation of the triclusters. The continuous increase in the fraction of the triclustered MgSiO_3 melt at high pressures and temperatures thus needs to be taken into account in future modeling of properties of mantle melts in order to improve our understanding of the microscopic origins of the anomalous pressure dependence of solubility of elements (noble gases and volatiles) into silicate melts with pressure relevant to the Earth’s deep mantle and the geochemical and geophysical processes in the Earth’s interior (Lee et al. 2008b). Note that there are number of other possibilities that lead to the formation of the peak at ~ 545 eV (Yi and Lee 2012): the theoretical confirmation of this proposal for the formation of oxygen tricluster in the glasses remains to be explored (see section “Insights from quantum chemical calculations” for further details).

Carbon K -edge XRS study

Bonding changes in compressed graphite. Carbon is one of the most important elements in the Earth system. The carbon atoms in crystalline diamond are characterized by sp^3 -hybridized orbitals with all four valence electrons, forming ^{14}C atoms. The carbon atoms in crystalline graphite are characterized by sp^2 -hybridized orbitals forming ^{14}C atoms. Amorphous carbon consists of 100% sp^2 bonding at 1 atm and shows high thermal stability and chemical durability. Carbon K -edge XRS has been used to explore the pressure-induced bonding transitions in graphite under compression (Mao et al. 2003). Figure 14 shows the C K -edge X-ray Raman scattering spectra for graphite in horizontal and vertical directions with varying pressure where detailed characterization of carbon in sp^2 and sp^3 bonding under compression are revealed. The peaks labeled π^* and σ^* correspond to the $1s-\pi_g^*$ and $1s-\sigma_u^*$ transitions, respectively. The C K -edge XRS spectrum for the a -plane showed only carbon atoms with σ -bonding regardless of pressures. The c -axis spectrum showed π -bonding but its intensity decreases $\sim 50\%$ at pressure above ~ 17 GPa. After the transition, the σ^* bond intensity apparently increases at the expense of the π^* . The results confirm that the π -bonds between graphite layers convert to σ -bonds with increasing pressure. Combined with XRD results, the results showed that at high pressure above 17 GPa, bridging carbon between graphite layers form σ -bonds, while the nonbridging

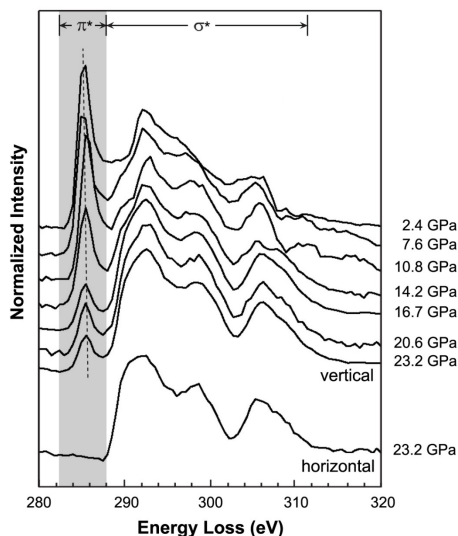


Figure 14. Carbon K -edge XRS spectra for graphite in horizontal and vertical directions with varying pressure. The spectrum is plotted as normalized scattered intensity vs. energy loss (incident energy – analyzer energy). The top seven spectra were collected by orienting the DAC to probe the bonds in the c plane (vertical direction, c axis parallel to the DAC axis) and the bottom spectra to probe bonds in the a plane (modified from Mao et al. 2003).

carbon remains unpaired. It was also reported that the high-pressure graphite phase is super hard, leading to a formation of indentations on the surface of diamond anvils (Mao et al. 2003).

Pressure-induced bonding changes in amorphous carbon allotrope. The pressure-induced bonding transitions in amorphous carbon forming diamond-like amorphous carbon were probed using XRS (Lin et al. 2011). Figure 15 shows C *K*-edge XRS spectra for amorphous carbon with varying pressure (compression and decompression as labeled). The peak at ~285 eV corresponds to the $1s$ to antibonding π^* transition, and the broad band at higher energy features the σ^* bonding (from $1s$ to σ^*). Upon compression, the XRS spectra show a gradual decrease in the π^* intensity and an increase in the σ^* peak. The C *K*-edge XRS spectrum for the amorphous carbon at ~44 GPa shows complete σ^* bonding, forming ^{14}C (and thus formation of a 100% sp^3 -bonded carbon). Upon decompression, the π^* peak (sp^2 bonding) intensity gradually increases, indicating reversible sp^2 - sp^3 bonding transitions (Lin et al. 2011).

Nitrogen *K*-edge XRS study. Nitrogen *K*-edge XRS has been utilized to probe pressure-induced bonding changes in BN polymorphs (Meng et al. 2004): please note that boron *K*-edge XRS study of the same materials has been discussed previously (see section “Pressure-induced bonding transitions in crystalline boron nitride (BN)”). Here, we discuss the pressure-induced structural transitions in the BN polymorphs using nitrogen *K*-edge. Figure 16 shows N *K*-edge XRS spectra for BN with varying pressure. The XRS spectrum at 1 atm shows the π and σ bonds, characteristic of *h*-BN. The π and σ bonds show pressure-induced changes in edge features and intensities. After further compression to 14 GPa, formation of the new features at approximately 410 eV is indicative of a phase transition to a hexagonal close-packed wurtzite structure

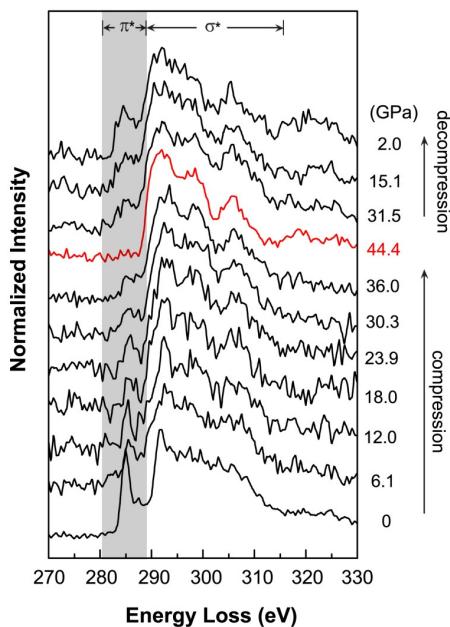


Figure 15. Carbon *K*-edge XRS spectra for amorphous carbon with varying pressure (as labeled compression and decompression). The spectra are plotted as normalized scattered intensity vs. energy loss (incident energy–analyzer elastic energy of 9.887 keV). Scattering angle of 30° was used (modified from Lin et al. 2011).

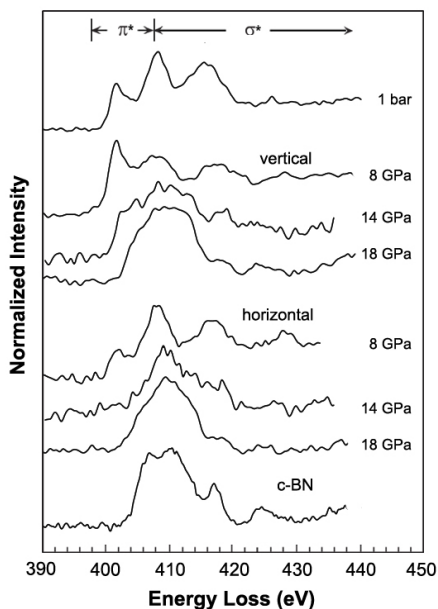


Figure 16. Nitrogen *K*-edge XRS spectra of BN with varying pressure. The spectra are plotted as normalized scattered intensity versus energy loss (incident energy – elastic energy) (modified from Meng et al. 2004).

(*w*-BN) (Meng et al. 2004). The overall similarity between the two electronic structures shown in the XRS spectra suggests that the bonding in *w*-BN is similar to that in *c*-BN: both *w*-BN and *c*-BN consist of *sp*³ bonding between B and N. Whereas detailed interpretation of XRS features necessitates the first principle calculations of the BN polymorphs, slight difference in XRS features for *w*-BN and *c*-BN phases indicates differences in their electronic density of states: the *c*-axis bond of *w*-BN has a more ionic nature than other bonds, while all bonds in *c*-BN are identical (Meng et al. 2004).

Helium K-edge XRS study: electronic structure of crystalline ⁴He at high pressures.

It is challenging to obtain an XRS signal for He due to overlap with other excitations and the backgrounds in the XRS spectra. However, a recent He *K*-edge study revealed the pressure-induced bonding transition in He (Mao et al. 2010): background from Be gasket spectrum and diamond spectrum were subtracted to yield the spectra shown in the figure (Mao et al. 2010). Figure 17 shows the He *K*-edge XRS spectrum for ⁴He with varying pressure. The edge features include an exciton peak at ~23-26 eV, a series of additional excitations and a continuum tail at 26 to 45 eV. At 11 GPa the He was compressed to form a hexagonal close-packed (hcp) He single crystal. The XRS spectrum of ⁴He at 13.4 GPa reveals a steep edge at ~23.7 eV, a sharp exciton peak at ~24.4 eV, a broad series of unresolved peaks at ~27.5 eV, and a continuum at higher energy. The presence of the broad peaks at 26-45 eV suggests the existence of the Wannier exciton (weakly bound electron-hole pair), in addition to the presence of the Frenkel exciton (tightly bound electron-hole pair) (Marder 2000; Mao et al. 2010).

Lithium K-edge XRS study: Pressure-induced structural transitions in Li in silicate glasses. In addition to intrinsic disorder associated with the distribution of network formers

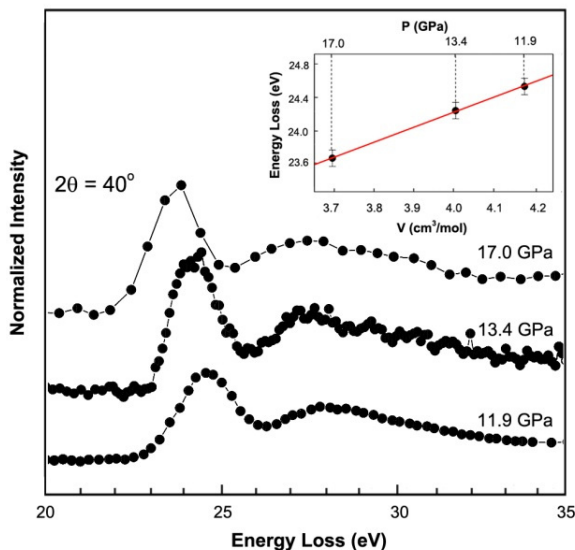


Figure 17. Helium *K*-edge XRS spectra for ⁴He sample with varying pressure (as labeled). The spectra are plotted as normalized scattered intensity vs. energy loss (incident energy–analyzer elastic energy). To get sufficient counting statistics, the authors were able to accumulate the signal and background from ⁴He for one month of beam time at 13ID-C of the GSECARS and 16ID-D [21] of the High Pressure Collaborative Access Team (HPCAT) at the Advanced Photon Source (APS), and the Taiwan Beamline BL12XU [20] at SPring-8, Japan. A scattering angle of 40° was used, which corresponds to momentum transfer *q* of 0.992, 0.998, and 0.972 for 11.9, 13.4, and 17, respectively. A panoramic DAC with large diamond anvils of 630 μm culet diameter was used. The exciton peak position with molar volume is also shown (inset) (modified from Mao et al. 2010).

(e.g., Si, Al, B, and Ti etc.), inherent structural disorder in the oxide glasses and melts includes topological disorder due to the distribution of cation-oxygen distance and bond angle variations involving network modifying cations (e.g., alkali and alkaline earth elements, such as Li, Na, Ca, Mg). The atomic environment of network modifying cations in oxide glasses is important for understanding transport properties including electric conductivity (Greaves and Ngai 1995; Jund et al. 2001; Lee and Stebbins 2003). Li *K*-edge studies have been utilized to probe electronic structures around Li in the crystalline oxides at 1 atm (Krisch et al. 1997; Sandi et al. 1998; Bergmann et al. 2002a; Tsuji et al. 2002). The coordination environment for Li in borate glasses has been recently studied using Li *K*-edge XRS up to 5 GPa (Lee et al. 2007).

Figure 18 presents Li *K*-edge XRS spectrum for Li-borate glasses at 5 GPa (Lee et al. 2007). The result shows XRS features similar to that at 1 atm. Note that the broad Be plasmon feature (inset), due to Be gasket used in the DAC, complicates Li *K*-edge spectrum. Nevertheless, the Be plasmon was effectively subtracted. Two weak features around 60 and 63 eV were observed. The features are similar to those reported for crystalline Li-halides and Li-silicates and are due to a transition from *1s* core electrons to valence band free orbitals (Bergmann et al. 2002b; Tsuji et al. 2002). The Li *K*-edge XRS spectra at 1 atm and 5 GPa are rather similar as expected from the similarity in the B *K*-edge XRS spectra measured at similar pressure ranges (Lee et al. 2007).

Insights from quantum chemical calculations

Experimental XRS studies have provided detailed information on pressure-induced bonding transitions in crystalline and amorphous earth materials at pressures up to ~70 GPa [e.g., 50 GPa for the O *K*-edge of SiO₂ glass (Lin et al. 2007), ~39 GPa for the O *K*-edge of MgSiO₃ glass (Lee et al. 2008b), ~74 GPa for the Si *L*-edge of SiO₂ glass (Fukui et al. 2008)]. The current pressure limit of ~40-70 GPa for XRS experiment (mostly limited by X-ray beam size and scattering geometry with the diamond anvil cell) poses a challenge to probing the detailed bonding environments in diverse silicate polymorphs stable above ~70 GPa. For example, because one of the important oxide phases in the Earth's mantle, MgSiO₃ post-perovskite (PPv) is stable near the core-mantle boundary at a pressure of ~120-135 GPa. The electronic bonding nature of the phase cannot be experimentally probed using current *in situ* high-pressure XRS experimental techniques.

For the analysis of XRS features, inputs from *ab initio* calculations (cf., Jahn and Kowalski 2014, this volume) are often necessary to establish the relationship between atomic configurations and edge features. Theoretical calculations (e.g., *ab initio* calculations) allow us to predict XRS spectra (or any core electron excitation spectroscopy, energy loss near edge spectroscopy) for crystalline oxides at high pressure, overcoming the current difficulties of *in situ* high-pressure experiments (Lin et al. 2007; Aryal et al. 2008; Meng et al. 2008; Fukui et al. 2009). Typical core electron excitation spectra (e.g., XAS, XRS, and EELS) for earth materials with low-*z* element have traditionally been calculated using multiple scattering theory. The method has been

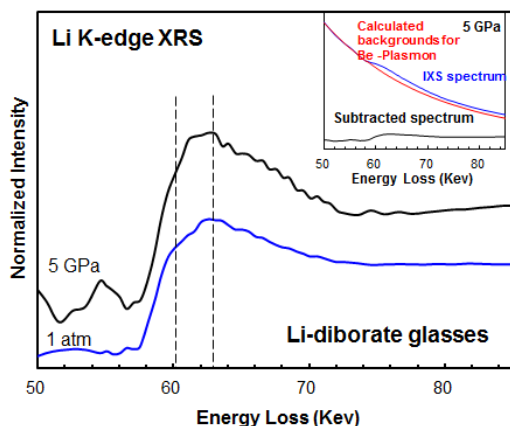


Figure 18. Lithium *K*-edge XRS spectra for Li-B₂O₃ glasses at 1 atm and 5 GPa. The inset shows the Be plasmon background subtraction methods for XRS spectra at 5 GPa: a contribution from the Be plasmon was fitted using a complex polynomial function and then subtracted from the spectrum (modified from Lee et al. 2007).

useful for reproducing the core-electron excitation spectrum for high- z elements (Wu et al. 1997; Cabaret et al. 1998; Rehr and Albers 2000; Krayzman et al. 2006; Eustace et al. 2010; Jorissen and Rehr 2010; Rehr et al. 2010) but it has met with limited success for calculations of spectra involving low- z elements (e.g., see Rehr and Albers 2000, de Groot 2001 and references therein for detailed discussion as well as the previous theoretical efforts on oxides). *Ab initio* DFT theory has been effective in calculation of core-electron excitation spectrum for low- z elements such as silicate oxides (Rez et al. 1999; Mizoguchi et al. 2000; Mo and Ching 2000; Schwarz et al. 2002; Tanaka et al. 2002; Ikeno et al. 2004; Kim et al. 2005; Cabaret et al. 2007; Sakko et al. 2007, 2010; Fukui et al. 2009; McLeod et al. 2010). The core-hole effect from the $1s$ -orbital of oxygen needs to be taken into consideration for the calculations of XRS spectra involving low- z elements (Tamura et al. 1995; Prewitt and Downs 1998; Mizoguchi et al. 2000; Luitz et al. 2001; Hebert et al. 2003; Hebert 2007). For example, O K -edge XRS experiments for SiO_2 polymorphs were well-reproduced by the oxygen $2p$ -projected electronic PDOS (e.g., Fukui et al. 2009 and references therein). The theoretical implementation of full-potential linearized augmented plane wave (FP-LAPW) methods have been effective in reproducing experimental XAS (and thus XRS) spectra for metal and simple phases (Blaha 2001; Hebert et al. 2003; Hebert 2007; Jorissen 2007; Fukui et al. 2009): Note again that XAS and XRS provide similar spectra under the dipole approximation (see “*Comparison with other core-electron excitation spectroscopy and traditional experimental probes at high pressure*” section above). The O K -edge XAS spectra of crystalline GeO_2 was successfully reproduced by the calculated theoretical spectra (Cabaret et al. 2007). Recent theoretical calculations of the O K -edge XRS features of SiO_2 glass at high pressure give insights into its densification mechanisms (Wu et al. 2012). These advances have recently been applied to calculate O K -edge XRS spectra for MgSiO_3 perovskite and post-perovskite) and those for dense oxygen crystals. The relevant results are briefly summarized below.

The electronic origins of XRS features in the ϵ -phase of oxygen with pressure were explored using *ab initio* calculations (Meng et al. 2008). Figure 19 shows the calculated O K -edge XRS spectra with increasing pressures from 10 to 47 GPa (Meng et al. 2008). With increasing pressure, both π^* and σ^* peaks moves to higher energy, consistent with the XRS experiments (Meng et al. 2008). A continuous decrease in π^* intensity in the ϵ -phase with

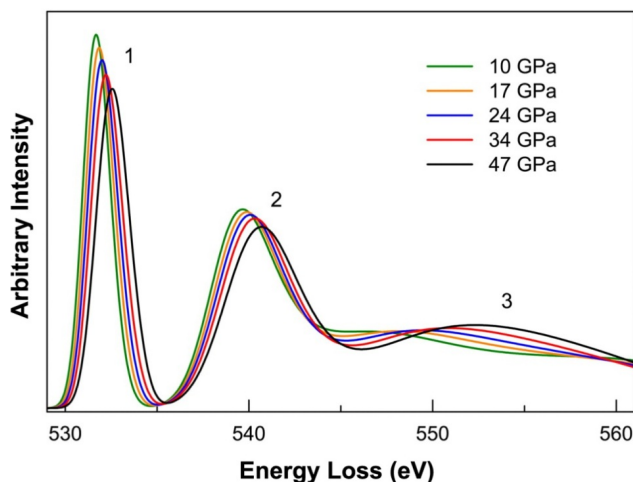


Figure 19. Calculated oxygen K -edge XRS spectra of the ϵ -phase with varying pressure as labeled. Peaks labeled as ‘1’, ‘2’, and ‘3’ correspond to contribution from electronic transitions of $1s$ electron to π^* , σ^* , and the continuum states, respectively (modified from Meng et al. 2009).

pressure indicates an increase in the π orbital delocalization. The results suggest an increase in the intercluster interaction with pressure in the ϵ -phase. With further increase in pressure the broad feature at ~ 550 eV stemming from the σ^* -like continuum state increases, suggesting prevalence of intercluster interaction in the ϵ -phase. We also note that similar *ab initio* methods have been applied to reproduce oxygen *K*-edge XRS spectra for SiO_2 glass with varying pressure. The results revealed that the pressure-induced structural transitions in Si coordination number can also affect the energy shift in the O *K*-edge XRS features (Wu et al. 2012).

Direct probing of the local electronic structure of mantle minerals, such as MgSiO_3 perovskite and post-perovskite, is challenging. The O *K*-edge XRS spectra for SiO_2 and MgSiO_3 polymorphs (i.e., α -quartz, stishovite, ortho-enstatite, ilmenite-type MgSiO_3 , MgSiO_3 perovskite, and post-perovskite) were calculated based on the FP-LAPW method to achieve improved insight into the origins of distinctive O *K*-edge features for MgSiO_3 polymorphs from their short-range structures and topology using the Wien2k code (Blaha 2001) (see Yi and Lee 2012 for computational details). Figure 20A shows the calculated O *K*-edge XRS spectrum for MgSiO_3 PPv. Two crystallographically distinct oxygen sites of MgSiO_3 PPv are a corner-sharing oxygen atom, $^{16}\text{Si-O1-}^{16}\text{Si}$ [O1 site], and an edge-sharing oxygen atom, $^{16}\text{Si-O2-}^{16}\text{Si}$ [O2 site], as shown in Figure 20B. The full spectrum was calculated by combining the results from these two sites. Both the O1 and O2 sites of MgSiO_3 PPv yield characteristic O *K*-edge features as shown in Figure 20C. Figure 20D shows the calculated PDOS for oxygen, confirming that the oxygen *2p*-state component contributes to the overall shape of the total O *K*-edge XRS spectrum (Yi and Lee 2012).

Figure 21 shows the calculated O *K*-edge XRS spectra for SiO_2 and MgSiO_3 polymorphs (Yi and Lee 2012). The calculated spectra are consistent with the experimental O *K*-edge XRS (red) spectra (Lin et al. 2007; Lee et al. 2008b) (see section “X-ray-induced dissociation of H_2O and formation of an $\text{O}_2\text{-H}_2$ alloy at high pressure” above). While future XRS experimental confirmation for MgSiO_3 PPv with improved X-ray optics and photon flux remains to be explored, the spectrum is expected to be similar to the calculated O *K*-edge XRS spectrum for MgSiO_3 PPv shown here.

The *ab initio* calculations provide crystallographic site-specific analysis of O *K*-edge features (Yi and Lee 2012). Figure 22 presents the calculated O *K*-edge XRS spectra for MgSiO_3 polymorphs (Yi and Lee 2012). It is clear that the O *K*-edge spectrum shift to higher energy ($\sim 3\text{-}4$ eV) with increasing degree of densification in atomic arrangement in MgSiO_3 polymorphs (from enstatite to PPv) (Fig. 22A). O *K*-edge features for the corner-sharing oxygen moves to higher energy from enstatite to PPv (121 GPa) (Fig. 22B). The features are mainly affected by the silicon coordination environment, O-O proximity, and Si-O bond lengths. A peak shift for edge-sharing oxygens in ilmenite- MgSiO_3 and PPv is also observed (Fig. 22C). A similar trend in pressure-induced edge energy shift has been reported for simple elements (e.g., O, Ne, and Cl), solid oxygen, as well as archetypal single component oxide glasses (see section “Oxygen *K*-edge XRS study of archetypal oxide glasses (SiO_2 , GeO_2 , and B_2O_3) at high pressure” above) (Cruz et al. 2005; Lin 2007).

Figure 23 shows the O *K*-edge XRS spectra for MgSiO_3 glass at 1 atm and 39 GPa compared with the calculated O *K*-edge features for MgSiO_3 Pv and PPv. The O *K*-edge feature for MgSiO_3 glass at ~ 39 GPa is comparable to the changes in the O *K*-edge features of MgSiO_3 Pv and PPv. The spectral differences between the local oxygen configurations of MgSiO_3 Pv and PPv and the changes in the O *K*-edge features imply that a densification of crystalline silicates (via formation of highly coordinated Si and enhanced proximity between oxygen atoms) leads to a shift of edge features into higher energy region.

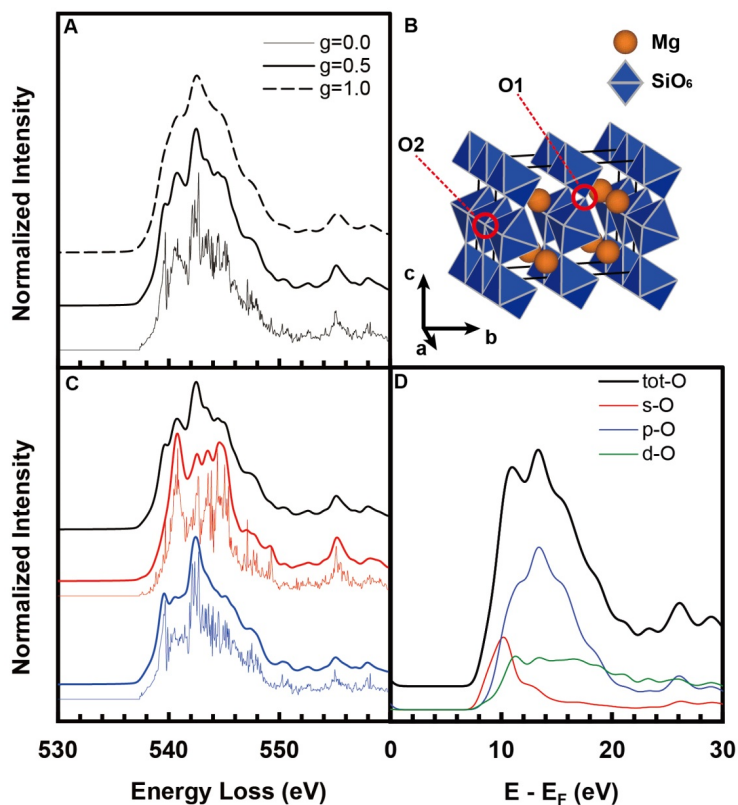


Figure 20. (A) Calculated oxygen *K*-edge XRS spectra for MgSiO₃ Post-Perovskite (PPv); the spectrometer broadening parameters (*g*) for Gaussian broadening FWHM are 0.0 eV (thin black solid), 0.5 eV (black solid), and 1.0 eV (black dashed). (B) The crystal structure of MgSiO₃ PPv and the crystallographically distinct oxygen sites (O1, corner-sharing oxygen; O2, edge-sharing oxygen). (C) O *K*-edge XRS spectra for MgSiO₃ PPv for each oxygen site and total O *K*-edge XRS spectrum (black solid), corner-sharing oxygen (O1, red solid), and edge-sharing oxygen (O2, blue solid). The Gaussian broadening (*g*) FWHM of 0.5 eV is used. (D) PDOS for each orbital of MgSiO₃ PPv. The Gaussian broadening FWHM for PDOS is 0.04 Ry (red solid, oxygen *s*-state; blue solid, oxygen *p*-state; green solid, oxygen *d*-state; black solid, total DOS of oxygen); the crystal structure of MgSiO₃ PPv is shown in the inset (Modified from Yi and Lee 2012). Quantum chemical calculations were performed using the Wien2k code, which utilizes a full-potential linear augmented plane wave plus local orbital methods (FP-LAPW+lo) (Blaha 2001). For computational details see Yi and Lee (2012).

REMAINING CHALLENGES AND OUTLOOK: APPLICATIONS OF NEW *K*-, *L*-, *M*-EDGE XRS, XRS WITH MOMENTUM TRANSFER, *IN SITU* HIGH-TEMPERATURE AND HIGH-PRESSURE XRS STUDY FOR MULTI-COMPONENTS GLASSES

In the previous sections, we have provided a summary of previous XRS studies on several popular *K*-edges (e.g., carbon, nitrogen, boron, oxygen) as well as less utilized *K*-edges (e.g., helium and lithium). Here, we briefly discuss additional XRS studies utilizing *L*- and *M*-edges for loosely bound electrons, XRS studies with momentum transfer, and XRS experiment involving multi-component oxide glasses. We then discuss other current and challenges and future studies.

Figure 21 (on left). Calculated O K-edge XRS spectra (black solid line) for SiO₂ (α -quartz, stishovite) and MgSiO₃ (ortho-enstatite, ilmenite, perovskite, and post-perovskite) polymorphs with the corresponding X-ray Raman scattering experimental results (open circles with solid line) from previous works (Lee et al. 2008b; Lin et al. 2007) (modified from Yi and Lee 2012).

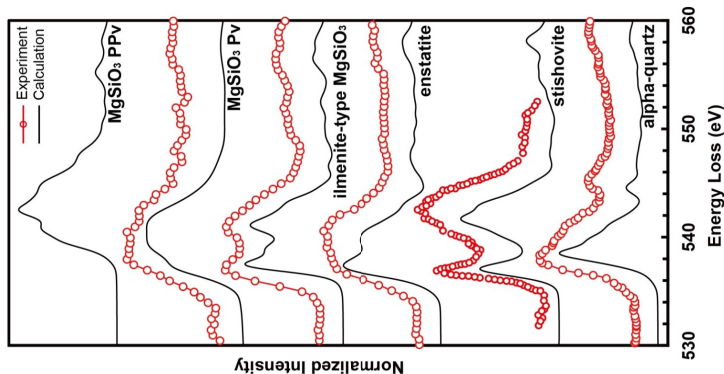


Figure 22 (on right). (A) Calculated O K-edge XRS spectra for MgSiO₃ high pressure polymorphs as labeled. (B) Calculated O K-edge XRS spectra for corner-sharing oxygen sites in MgSiO₃ high pressure polymorphs. (C) Calculated O K-edge XRS spectra for edge-sharing oxygen site in SiO₂ and MgSiO₃ polymorphs as labeled. The spectrometer broadening parameter (σ) of Gaussian broadening FWHM of 1.0 eV was used (modified from Yi and Lee 2012).

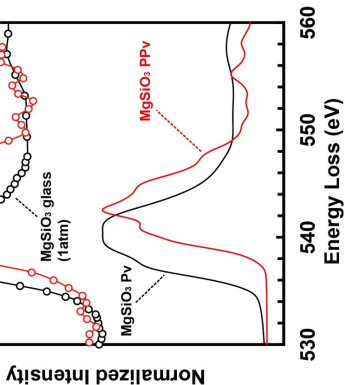
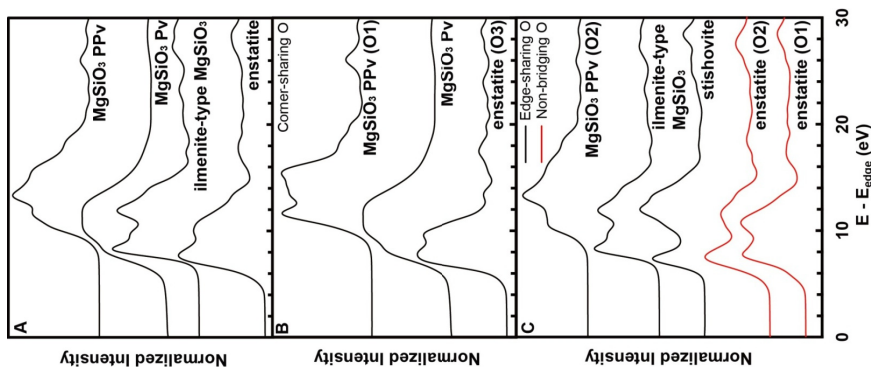


Figure 23 (above). Oxygen K-edge XRS spectra for MgSiO₃ glass at 1 atm and 39 GPa, and for MgSiO₃ perovskite and post-perovskite as labeled. The Gaussian broadening FWHM for the calculated O K-edge ELNES spectra is 1.0 eV (modified from Yi and Lee 2012).

Application of *L*- and *M*-edge XRS techniques to oxides and silicates under pressure

While the application of XRS can be effective for providing *element specific* information on atomic configurations, its application has focused on the low-*z* elements in the 2nd row of periodic table. Furthermore, the XRS features in the 10-100 eV region can be complicated by diverse sources of background signals (e.g., Compton scattering peak, Be plasmon) that overlap with the IXS features in these region. Be plasmon due to Be gasket can be effectively removed as shown in the previous Li *K*-edge study (Lee et al. 2007). As the Compton peak position moves to higher energy and its peak width gets broader with increasing scattering angle (2θ), the inelastic X-ray scattering spectrum within 10-100 eV region can be probed by carefully adjusting scattering angle and geometry (Lee et al. unpubl data). In Figure 2, we also showed Ca *M*-edges (20-40 eV) for Ca-silicate glasses. Similar approaches can be applied to diverse Ca-bearing silicates and oxide under extreme pressure. However, *L*-, *M*-, and *N*-edge XRS spectra for high-*z* elements have also provided useful information on electronic structures by probing excitations of electron from *p* and *d* orbitals to unbound states. The edges studied using XRS at 1 atm are the *L*-edges (from *2p* to virtual states) of Na, Si, and Ba, *M*-edges (from *3p* to virtual states) of *3d* metals, *N*-edges (from *4d* to unbound states) features of barium, lanthanum and cerium materials, and *O*-edges (from *5d* to unbound states) features from compounds consisting of actinides (see Sternemann et al. 2007a,b and Gordon et al. 2011 and references therein). The application of these edges focused on the structure of simple systems at 1 atm. With a possible exception of a recent Si *L*-edge (~120 eV) study of SiO₂ glasses under pressure above 70 GPa (Fukui et al. 2008), these edges have not been explored for the silicates and oxides at high pressure.

In order to explore the pressure-induced changes in the structure of network modifying cations in silicate glasses at high pressure, Ca *L*-edge XRS spectrum for CaSiO₃ glass at 1 atm and 21 GPa are presented (Fig. 24). The two features at ~349 and 353 eV are due to an excitation of an electron from the Ca *2p*-state with total angular momentum of 3/2 and 1/2 into unoccupied states (labeled as, *L*₃, *L*₂ transitions), respectively (cf., Henderson et al. 2013). The *L*₃/*L*₂ ratio at high pressure is somewhat smaller than that at 1 atm: because the signal to background (S/B) ratio is low for the spectrum at high pressure, the change in *L*₃/*L*₂ ratio may result from spectral uncertainty. However, the change could also imply structural changes (e.g., average coordination number) around Ca in the glasses at high pressure. Furthermore, it may suggest the presence of a potential spin transition (from high spin (*L*₃) to low spin (*L*₂)) at pressure. Further experimental and theoretical efforts are necessary to provide atomistic origins of the change.

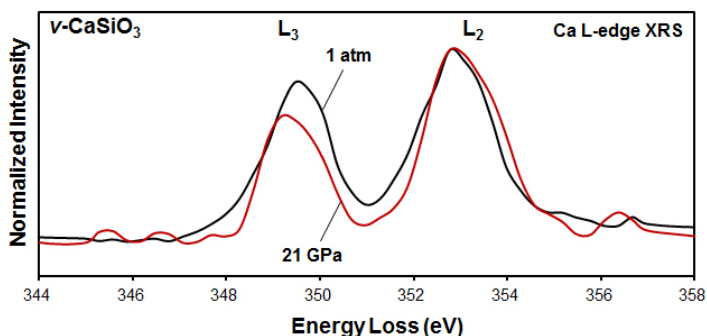


Figure 24. Calcium *L*-edge XRS spectrum for CaSiO₃ glass with varying pressure. The features at ~349 and 353 eV are due to an excitation of a core electron from the Ca *2p*-state with total angular momentum of 3/2 and 1/2 into unoccupied states (labeled as, *L*₃, *L*₂ transitions), respectively.

Application of XRS technique to multi-component oxide glasses under pressure

While materials with relatively simple compositions (pure elements, single component and binary earth materials) have been thus far studied, further efforts to reveal the structures of multi-component earth materials are necessary to account for the variations in the properties of natural earth materials. Intrinsic disorder inherent in multicomponent (i.e., beyond quaternary) oxide glasses, however, makes it difficult to resolve their atomic structures at both ambient and elevated pressure conditions as peak overlap (or double differential scattering cross section) increases with increasing numbers of components. While this aspect could also pose a serious problem for any spectroscopic and scattering technique, an element specific like XRS could be potentially useful in revealing the densification mechanisms of these multi-component oxide glasses.

Indeed, XRS has been applied to probe local atomic configuration around oxygen in multi-component model basaltic glasses (Ca-Mg aluminosilicate melt of diopside-anorthite eutectic composition, $\text{Di}_{64}\text{An}_{36}$) at 1 atm and the glass under shock compression (Lee et al. 2012). The structures of shock compressed glasses are essential to understand the changes in the corresponding melt properties under dynamic compression and magmatic processes in the Earth's interior (Ahrens 1996; Okuno et al. 1999; Reynard et al. 1999; Akins et al. 2004; Shimoda et al. 2004; Tschauner et al. 2009). O *K*-edge XRS provides an opportunity to reveal the shock-induced transitions in atomic environments around oxygen in unshocked and shocked model basaltic glasses (Lee et al. 2012). Figure 25 shows the O *K*-edge X-ray Raman spectra for unshocked (black) and shocked $\text{Di}_{64}\text{An}_{36}$ glass (red spectrum) (Lee et al. 2012). A dominant peak at 538–540 eV is prevalent for both unshocked and shocked glass and is due to an excitation of a core electron from the oxygen 1*s*-state into unoccupied oxygen 2*p*-states stemming from four-coordinated Si atoms, similar to features in other silicate glasses at 1 atm (Lin et al. 2007; Lee et al. 2008b). Shock compression apparently leads to a slight edge energy shift (~1 eV). O *K*-edge features move to higher energy with an increasing degree of densification in Mg-silicate polymorphs due to an increase in the energy of unoccupied oxygen 2*p*-states (Yi and Lee 2012).

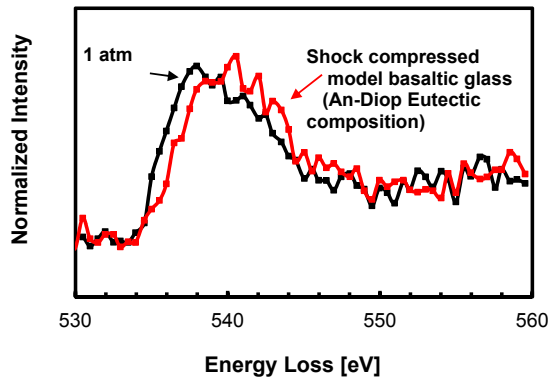


Figure 25. Oxygen *K*-edge XRS spectra for glass with a diopside–anorthite eutectic composition ($\text{Di}_{64}\text{An}_{36}$) quenched from melts at 1 atm and recovered after shock compression. The spectra were plotted as normalized scattered intensity vs. energy loss (incident energy – elastic energy). The X-ray Raman scattering spectra for the unshocked and shocked $\text{Di}_{64}\text{An}_{36}$ glass were collected at HPCAT sector 16ID-D of the APS. X-ray Raman spectra were collected for the samples (~200 μm) attached to 100- μm glass fibers mounted directly on the goniometer. The spectra were collected by scanning the energy of the incident beam relative to the analyzer with a fixed elastic energy (E_0) of ~9.886 keV at a scattering angle of 20°. A linear array of 17 spherical Si(555) analyzers operating in a backscattering geometry was used. The X-ray beam size was approximately 50 μm (H) \times 30 μm (V) (modified from Lee et al. 2012).

The current result thus suggests a densification of the $\text{Di}_{64}\text{An}_{36}$ glass upon shock compression. We note that due to the pronounced uncertainty in spectral features (stemming from low signal/background ratio of the spectrum and insufficient signal averaging), the observed shift should not be regarded as strong evidence for noticeable structural transitions (e.g., coordination number of Si) after shock-compression but may result from mostly topological changes (bond angle and lengths and medium-range structure) (Lee et al. 2012).

Application of new *K*-edges (elements in the 3rd row of the periodic table) and momentum transfer XRS to crystals under pressure

The XRS signal intensity tends to decrease with increasing atomic number of elements (e.g., Na, Mg) and thus it is still a challenge to collect sufficiently high quality XRS spectra for Na and Mg in silicates and oxides. Note that Na *K*-edge XRS has probed the electronic structures of NaCl and NaF (Nagle et al. 2009). These edges have not been utilized for oxides and silicates at 1 atm so far but the edge features will be potentially useful to probe the local structure of other Na compounds as well as Na-bearing silicate glasses and minerals. Its application to diverse glasses and crystals at high pressure also remains to be explored. Additionally, revealing the momentum-transfer dependent edge feature can provide studies of non-dipole transitions in materials (Caliebe et al. 2000; Hamalainen et al. 2002; Soininen et al. 2006; Gordon et al. 2011). This aspect has not been fully utilized for the study of earth materials under pressure but is potentially useful in resolving the detailed nature of bonding in iron bearing oxide glasses and/or transition metal sites in the earth materials.

***In situ* high-temperature and high-pressure XRS studies**

Further study of effect of high temperature is another target of future research. Current experiments are mostly for room temperature applications. The future development of measurement techniques (involving laser heating) operating at higher temperature ranges seems necessary to explore the effect of temperature on electronic bonding transitions in oxides under pressure. Conventional external heating and/or laser heating technique can be implemented with DAC, allowing us explore the effect of both temperature and pressure on electronic bonding simultaneously (Mao and Mao 2007)

Outlook and prospects

As XRS beamlines have been experiencing major experimental improvements and upgrades during the last couple of years in several synchrotron radiation sources, and technical advances with X-ray optics and DAC cell design are likely to be continued, development of efficient XRS protocols with improved DAC cell design and X-ray optics with better photon flux is certainly expected. These notable advances may also hold some promise for studying the structure of diverse earth materials under pressure. Additionally, because the application of XRS to earth materials at high pressure is relatively new and has only been applied to a limited number of earth materials, current XRS methods with ~ 1 eV resolution and with fluxes of $\sim 10^{13}$ photons/s/eV can still be extremely useful to probe structural transitions in oxide glasses and crystals under compression. While many challenges remain, the XRS technique is a promising tool for probing pressure-induced changes in detailed atomic structures at elevated pressures.

ACKNOWLEDGMENTS

This research was supported by National Research Foundation, Korea (2012-026-411) and partly supported by the Korea Meteorological Administration Research and Development Program under Grant CATER 2012-8030 to S.K. Lee. We are grateful for careful and constructive suggestions by Grant Henderson and two anonymous reviewers. We sincerely thank colleagues and collaborators, Jinfu Shu, Jung-Fu Lin, Yue Meng, Matt Newville, Wendy Mao, Paul Chow, Sun Young Park, Hyo-Im Kim, Oliver Tschauner, Paul Asimow, Ligang Bai, Yuming Xiao,

Hyunna Kim, Bum Han Lee, Yoosoo Yi, Yong Q. Cai, Nozomu Hiraoka, Takuo Okuchi, Michael Y. Hu, Paul Chow, Baosheng Li, Hiroshi Fukui, Yang Ding, Chicang Kao, John Tse, Yu Lin, and Choong-Shik Yoo for the invaluable contributions to the results presented here. GSECARS was supported by DOE-BES-Geosciences, NSF-Earth Sciences and the State of Illinois. HPCAT operations are supported by DOE-NNSA under Award No. DE-NA0001974 and DOE-BES under Award No. DE-FG02-99ER45775, with partial instrumentation funding by NSF. APS is supported by DOE-BES, under Contract No. DE-AC02-06CH11357. Lee SK thanks travel supports from LG fellowship.

REFERENCES

- Agee CB (2008) Static compression of hydrous silicate melt and the effect of water on planetary differentiation. *Earth Planet Sci Lett* 265:641-654
- Ahrens TJ (1996) Application of shock compression science to Earth and planetary physics. *In: Shock Compression of Condensed Matter*. Schmidt SCTWC (Ed) p 3-8
- Akins JA, Luo SN, Asimow PD, Ahrens TJ (2004) Shock-induced melting of MgSiO_3 perovskite and implications for melts in Earth's lowermost mantle. *Geophys Res Lett* 31:L14612
- Allwardt JR, Schmidt BC, Stebbins JF (2004) Structural mechanisms of compression and decompression in high pressure $\text{K}_2\text{Si}_4\text{O}_9$ glasses: An investigation utilizing Raman and NMR spectroscopy of high-pressure glasses and crystals. *Chem Geol* 213:137-151
- Allwardt JR, Poe BT, Stebbins JF (2005a) The effect of fictive temperature on Al coordination in high-pressure (10 GPa) sodium aluminosilicate glasses. *Am Mineral* 90:1453-1457
- Allwardt JR, Stebbins JF, Schmidt BC, Frost DJ, Withers AC, Hirschmann MM (2005b) Aluminum coordination and the densification of high-pressure aluminosilicate glasses *Am Mineral* 90:1218-1222
- Angell CA, Cheeseman PA, Tamaddon S (1982) Pressure enhancement of ion mobilities in liquid silicates from computer simulations studies to 800 kbar. *Science* 218:885-887
- Aryal S, Rulis P, Ching WY (2008) Density functional calculations of the electronic structure and optical properties of aluminosilicate polymorphs (Al_2SiO_5). *Am Mineral* 93:114-123
- Bergmann U, Mullins OC, Cramer SP (2000) X-ray Raman spectroscopy of carbon in asphaltene: Light element characterization with bulk sensitivity. *Anal Chem* 72:2609-2612
- Bergmann U, Glatzel P, Cramer SP (2002a) Bulk-sensitive XAS characterization of light elements: from X-ray Raman scattering to X-ray Raman spectroscopy. *Microchem J* 71:221-230
- Bergmann U, Wernet P, Glatzel P, Cavalleri M, Pettersson LGM, Nilsson A, Cramer SP (2002b) X-ray Raman spectroscopy at the oxygen K edge of water and ice: Implications on local structure models. *Phys Rev B* 66:092107
- Bergmann U, Groenzin H, Mullins OC, Glatzel P, Fetzter J, Cramer SP (2003) Carbon K-edge X-ray Raman spectroscopy supports simple, yet powerful description of aromatic hydrocarbons and asphaltenes. *Chem Phys Lett* 369:184-191
- Bergmann U, Groenzin H, Mullins OC, Glatzel P, Fetzter J, Cramer SP (2004) X-ray Raman spectroscopy - A new tool to study local structure of aromatic hydrocarbons and asphaltenes. *Pet Sci Technol* 22:863-875
- Blaaha P, Schwarz K, Madsen G, Kvasnicka D, Luitz J (2001) WIEN2k. *Techn. Univ. Wien, Austria, Wien*.
- Bowron DT, Krisch MH, Barnes AC, Finney JL, Kaprolat A, Lorenzen M (2000) X-ray-Raman scattering from the oxygen K edge in liquid and solid H_2O . *Phys Rev B* 62:R9223-R9227
- Brown GE Jr, Farges F, Calas G (1995) X-ray scattering and X-ray spectroscopy studies of silicate melts. *Rev Mineral Geochem* 32:317-410
- Brydson R, Brown A, Benni LG, Livi K (2014) Analytical transmission electron microscopy. *Rev Mineral Geochem* 78:219-269
- Cabaret D, Sainctavit P, Ildefonse P, Flank AM (1998) Full multiple scattering calculations of the X-ray absorption near edge structure at the magnesium K-edge in pyroxene. *Am Mineral* 83:300-304
- Cabaret D, Mauri F, Henderson GS (2007) Oxygen K-edge XANES of germanates investigated using first-principles calculations. *Phys Rev B* 75:184205
- Cai YQ, Mao HK, Chow PC, Tse JS, Ma Y, Patchkovskii S, Shu JF, Struzhkin V, Hemley RJ, Ishii H, Chen CC, Jarrige I, Chen CT, Shieh SR, Huang EP, Kao CC (2005) Ordering of hydrogen bonds in high-pressure low-temperature H_2O . *Phys Rev Lett* 94:025502
- Caliebe WA, Soininen JA, Shirley EL, Kao CC, Hamalainen K (2000) Dynamic structure factor of diamond and LiF measured using inelastic X-ray scattering. *Phys Rev Lett* 84:3907-3910
- Caracas R, Cohen RE (2006) Theoretical determination of the Raman spectra of MgSiO_3 perovskite and post-perovskite at high pressure. *Geophys Res Lett* 33:L12S05

- Chan MKY, Shirley EL, Karan NK, Balasubramanian M, Ren Y, Greeley JP, Fister TT (2011) Structure of Lithium Peroxide. *J Phys Chem Lett* 2:2483-2486
- Cruz SA, Díaz-García C, Pathak AP, Soullard J (2005) Pressure dependence of the mean excitation energy of atomic systems. *Nucl Instrum Methods B* 230:46-52
- Davoli I, Paris E, Stizza S, Benfatto M, Fanfoni M, Gargano A, Bianconi A, Seifert F (1992) Structure of identified vitreous silica - silicon and oxygen Xanes spectra and multiple-scattering calculations. *Phys Chem Miner* 19:171-175
- de Groot F (2001) High resolution X-ray emission and X-ray absorption spectroscopy. *Chem Rev* 101:1779-1808
- Diefenbacher J, McMillan PF, Wolf GH (1998) Molecular dynamics simulations of $\text{Na}_2\text{Si}_4\text{O}_9$ liquid at high pressure. *J Phys Chem B* 102:3003-3008
- Eckert H (1992) Structural characterization of noncrystalline solids and glasses using solid state NMR. *Prog Nucl Mag Reson* 24:159-293
- Eustace DA, McComb DW, Craven AJ (2010) Probing magnetic order in EELS of chromite spinels using both multiple scattering (FEFF8.2) and DFT (WIEN2k). *Micron* 41:547-553.
- Feng YJ, Soininen JA, Ankudinov AL, Cross JO, Seidler GT, Macrander AT, Rehr JJ, Shirley EL (2008) Exciton spectroscopy of hexagonal boron nitride using nonresonant X-ray Raman scattering. *Phys Rev B* 77:165202
- Fister TT, Seidler GT, Wharton L, Battle AR, Ellis TB, Cross JO, Macrander AT, Elam WT, Tyson TA, Qian Q (2006) Multielement spectrometer for efficient measurement of the momentum transfer dependence of inelastic X-ray scattering. *Rev Sci Instrum* 77:063901
- Fister TT, Seidler GT, Rehr JJ, Kas JJ, Elam WT, Cross JO, Nagle KP (2007) Deconvolving instrumental and intrinsic broadening in core-shell X-ray spectroscopies. *Phys Rev B* 75:174106
- Fister TT, Seidler GT, Shirley EL, Vila FD, Rehr JJ, Nagle KP, Linehan JC, Cross JO (2008a) The local electronic structure of $\alpha\text{-Li}_3\text{N}$. *J Phys Chem* 129:044702
- Fister TT, Vila FD, Seidler GT, Svec L, Linehan JC, Cross JO (2008b) Local electronic structure of dicarbocloso-dodecaboranes $\text{C}_2\text{B}_{10}\text{H}_{12}$. *J Am Chem Soc* 130:925-932
- Fister TT, Nagle KP, Vila FD, Seidler GT, Hamner C, Cross JO, Rehr JJ (2009a) Intermediate-range order in water ices: Nonresonant inelastic X-ray scattering measurements and real-space full multiple scattering calculations. *Phys Rev B* 79:174117
- Fister TT, Fong DD, Eastman JA, Iddir H, Zapol P, Fuoss PH, Balasubramanian M, Gordon RA, Balasubramanian KR, Salvador PA (2011a) Total-reflection inelastic X-Ray scattering from a 10-nm thick $\text{La}_{0.6}\text{Sr}_{0.4}\text{CoO}_3$ thin film. *Phys Rev Lett* 106:037401
- Fister TT, Schmidt M, Fenter P, Johnson CS, Slater MD, Chan MKY, Shirley EL (2011b) Electronic structure of lithium battery interphase compounds: comparison between inelastic X-ray scattering measurements and theory. *J Phys Chem* 135:224513-224513
- Fleet ME, Muthupari S (1999) Coordination of boron in alkali borosilicate glasses using XANES. *J Non-Cryst Solids* 255:233-241
- Fleet ME, Muthupari S (2000) Boron K-edge XANES of borate and borosilicate minerals. *Am Mineral* 85:1009-1021
- Fukui H, Kanzaki M, Hiraoka N, Cai YQ (2008) Coordination environment of silicon in silica glass up to 74 GPa: An X-ray Raman scattering study at the silicon L-edge. *Phys Rev B* 78:012203
- Fukui H, Kanzaki M, Hiraoka N, Cai YQ (2009) X-ray Raman scattering for structural investigation of silica/silicate minerals. *Phys Chem Miner* 36:171-181
- Garvie LAJ, Rez P, Alvarez JR, Buseck PR, Craven AJ, Brydson R (2000) Bonding in α -quartz (SiO_2): A view of the unoccupied states. *Am Mineral* 85:732-738
- Garvie LAJ, Craven AJ (1995) Parallel electron energy-loss spectroscopy (PEELS) study of B in minerals: The electron energy-loss near edge structure (ELNES) of the B K-edge. *Am Mineral* 80:1132-1144
- Gordon ML, Tulumello D, Cooper G, Hitchcock AP, Glatzel P, Mullins OC, Cramer SP, Bergmann U (2003) Inner-shell excitation spectroscopy of fused-ring aromatic molecules by electron energy loss and X-ray Raman techniques. *J Phys Chem A* 107:8512-8520
- Gordon RA, Seidler GT, Fister TT, Nagle KP (2011) Studying low-energy core-valence transitions with bulk sensitivity using q-dependent NIXS. *J Electron Spectrosc* 184:220-223
- Greaves GL, Ngai KL (1995) Reconciling ionic-transport properties with atomic-structure in oxide glasses. *Phys Rev B* 52:6358-6380
- Hamalainen K, Galambosi S, Soininen JA, Shirley EL, Rueff JP, Shukla A (2002) Momentum dependence of fluorine K-edge core exciton in LiF. *Phys Rev B* 65:155111
- Hebert C (2007) Practical aspects of running the WIEN2k code for electron spectroscopy. *Micron* 38:12-28
- Hebert C, Luitz J, Schattschneider P (2003) Improvement of energy loss near edge structure calculation using Wien2k. *Micron* 34:219-225
- Hemley RJ (ed) (1998) *Ultra-high-Pressure Mineralogy: Physics and Chemistry of the Earth's Deep Interior*. Reviews in Mineralogy 37. Mineralogical society of America, Washington, DC

- Henderson GS, Neuville DR, Cormier L (2009) An O K-edge XANES study of glasses and crystals in the CaO-Al₂O₃-SiO₂ (CAS) system. *Chem Geol* 259:54-62
- Henderson GS, de Groot FMF, Moulton BJA (2014) X-ray absorption near-edge structure (XANES) spectroscopy. *Rev Mineral Geochem* 78:75-138
- Ikeno H, Tanaka I, Miyamae L, Mishima T, Adachi H, Ogasawara K (2004) First principles calculation of Fe L_{2,3}-edge X-ray absorption near edge structures of iron oxides. *Mater Trans* 45:1414-1418
- Jahn S, Kowalski PM (2014) Theoretical approaches to structure and spectroscopy of earth materials. *Rev Mineral Geochem* 78:691-743
- Jorissen K (2007) The ab initio Calculation of Relativistic Electron Energy Loss Spectra. Department of Physics, Doctor of Philosophy. University of Antwerp.
- Jorissen K, Rehr JJ (2010) Calculations of electron energy loss and X-ray absorption spectra in periodic systems without a supercell. *Phys Rev B* 81:245124
- Jund P, Kob W, Jullien R (2001) Channel diffusion of sodium in a silicate glass. *Phys Rev B* 64:4303-4308.
- Karan NK, Balasubramanian M, Fister TT, Burrell AK, Du P (2012) Bulk-sensitive characterization of the discharged products in Li-O-2 batteries by nonresonant inelastic X-ray scattering. *J Phys Chem C* 116:18132-18138
- Kelsey KE, Stebbins JF, Mosenfelder JL, Asimow PD (2009a) Simultaneous aluminum, silicon, and sodium coordination changes in 6 GPa sodium aluminosilicate glasses. *Am Mineral* 94:1205-1215
- Kelsey KE, Stebbins JF, Singer DM, Brown GE Jr, Mosenfelder JL, Asimow PD (2009b) Cation field strength effects on high pressure aluminosilicate glass structure: Multinuclear NMR and La XAFS results. *Geochim Cosmochim Acta* 73:3914-3933
- Kim S, Kim Y, Hong J, Tanaka I, No K (2005) Electronic structure and X-ray-absorption near-edge structure of amorphous Zr-oxide and Hf-oxide thin films: A first-principles study. *J Appl Phys* 97:073519
- Krayzman V, Levin I, Woicik JC, Yoder D, Fischer DA (2006) Effects of local atomic order on the pre-edge structure in the Ti K X-ray absorption spectra of perovskite CaTi_{1-x}Zr_xO₃. *Phys Rev B* 74:224104
- Krisch MH, Sette F, Masciovecchio C, Verbeni R (1997) Momentum transfer dependence of inelastic X-ray scattering from the Li K-edge. *Phys Rev Lett* 78:2843-2846
- Laudernet Y, Clerouin J, Mazevet S (2004) Ab initio simulations of the electrical and optical properties of shock-compressed SiO₂. *Phys Rev B* 70:165108
- Lee SK (2005) Microscopic origins of macroscopic properties of silicate melts: implications for melt generation and dynamics. *Geochim Cosmochim Acta* 69:3695-3710
- Lee SK (2010) Effect of pressure on structure of oxide glasses at high pressure: Insights from solid-state NMR of quadrupolar nuclides. *Solid State Nucl Magn Reson* 38:45-57
- Lee SK (2011) Simplicity in melt densification in multi-component magmatic reservoirs in Earth's interior revealed by multi-nuclear magnetic resonance. *Proc Natl Acad Sci USA* 108:6847-6852
- Lee SK, Stebbins JF (2003) The distribution of sodium ions in aluminosilicate glasses: A high field Na-23 MAS and 3QMAS NMR study. *Geochim Cosmochim Acta* 67:1699-1709
- Lee SK, Fei Y, Cody GD, Mysen BO (2003) Order and disorder of sodium silicate glasses and melts at 10 GPa. *Geophys Res Lett* 30:1845
- Lee SK, Eng PJ, Mao HK, Meng Y, Newville M, Hu MY, Shu JF (2005) Probing of bonding changes in B₂O₃ glasses at high pressure with inelastic X-ray scattering. *Nat Mater* 4:851-854
- Lee SK, Eng PJ, Mao HK, Meng Y, Shu J (2007) Structure of alkali borate glasses at high pressure: B and Li K-edge inelastic X-ray scattering study. *Phys Rev Lett* 98:105502
- Lee SK, Eng P, Mao HK, Shu JF (2008a) Probing and modeling of pressure-induced coordination transformation in borate glasses: Inelastic X-ray scattering study at high pressure. *Phys Rev B* 78:214203
- Lee SK, Lin JF, Cai YQ, Hiraoka N, Eng PJ, Okuchi T, Mao HK, Meng Y, Hu MY, Chow P, Shu JF, Li BS, Fukui H, Lee BH, Kim HN, Yoo CS (2008b) X-ray Raman scattering study of MgSiO₃ glass at high pressure: Implication for triclustered MgSiO₃ melt in Earth's mantle. *Proc Natl Acad Sci USA* 105:7925-7929
- Lee SK, Park SY, Kim H-I, Tschauner O, Asimow P, Bai LG, Xiao YM, Chow P (2012) Structure of shock compressed model basaltic glass: Insights from O K-edge X-ray Raman scattering and high-resolution Al-27 NMR spectroscopy. *Geophys Res Lett* 39:L05306
- Lelong G, Cormier L, Ferlat G, Giordano V, Henderson GS, Shukla A, Calas G (2012) Evidence of fivefold-coordinated Ge atoms in amorphous GeO₂ under pressure using inelastic X-ray scattering. *Phys Rev B* 85:134202
- Lin JF, Fukui H, Prendergast D, Okuchi T, Cai YQ, Hiraoka N, Yoo CS, Trave A, Eng P, Hu MY, Chow P (2007) Electronic bonding transition in compressed SiO₂ glass. *Phys Rev B* 75:012201
- Lin Y, Zhang L, Mao HK, Chow P, Xiao YM, Baldini M, Shu JF, Mao WL (2011) Amorphous Diamond: A High-Pressure Superhard Carbon Allotrope. *Phys Rev Lett* 107:175504
- Luitz J, Maier M, Hebert C, Schattschneider P, Blaha P, Schwarz K, Jouffrey B (2001) Partial core hole screening in the Cu L₃-edge. *Eur Phys J B* 21:363-367
- Mao HK, Mao WL (2007) Theory and practice - diamond-anvil cells and probes for high P-T mineral physics studies. *In: Treatise on Geophysics*. Gerald S (Ed) Elsevier, Amsterdam. p 231-267

- Mao WL, Mao HK, Eng PJ, Trainor TP, Newville M, Kao CC, Heinz DL, Shu JF, Meng Y, Hemley RJ (2003) Bonding changes in compressed superhard graphite. *Science* 302: 425-427
- Mao WL, Mao HK, Meng Y, Eng PJ, Hu MY, Chow P, Cai YQ, Shu JF, Hemley RJ (2006) X-ray-induced dissociation of H₂O and formation of an O₂-H₂ alloy at high pressure. *Science* 314:636-638
- Mao HK, Shirley EL, Ding Y, Eng P, Cai YQ, Chow P, Xiao YM, Shu JF, Hemley RJ, Kao CC, Mao WL (2010) Electronic structure of crystalline He-4 at high pressures. *Phys Rev Lett* 105:186404
- Marder (2000) *Condensed Matter Physics*. John Wiley
- McLeod JA, Wilks RG, Skorikov NA, Finkelstein LD, Abu-Samak M, Kurmaev EZ, Moewes A (2010) Band gaps and electronic structure of alkaline-earth and post-transition-metal oxides. *Phys Rev B* 81:245123
- Meng Y, Mao HK, Eng PJ, Trainor TP, Newville M, Hu MY, Kao CC, Shu JF, Hausermann D, Hemley RJ (2004) The formation of sp(3) bonding in compressed BN. *Nat Mater* 3:111-114
- Meng Y, Eng PJ, Tse JS, Shaw DM, Hu MY, Shu JF, Gramsch SA, Kao C, Hemley RJ, Mao HK (2008) Inelastic X-ray scattering of dense solid oxygen: Evidence for intermolecular bonding. *Proc Natl Acad Sci USA* 105:11640-11644
- Micoulaut M, Cormier L, Henderson GS (2006) The structure of amorphous, crystalline and liquid GeO₂. *J Phys-Condens Mat* 18:R753-R784
- Mizoguchi T, Tanaka I, Yoshiya M, Oba F, Ogasawara K, Adachi H (2000) Core-hole effects on theoretical electron-energy-loss near-edge structure and near-edge X-ray absorption fine structure of MgO. *Phys Rev B* 61:2180
- Mizuno Y, Ohmura Y (1967) Theory of X-ray Raman scattering. *J Phys Soc Japan* 22:445-&
- Mo SD, Ching WY (2000) Ab initio calculation of the core-hole effect in the electron energy-loss near-edge structure. *Phys Rev B* 62:7901-7907
- Murakami M, Bass JD (2010) Spectroscopic evidence for ultrahigh-pressure polymorphism in SiO₂ glass. *Phys Rev Lett* 104:025504
- Mysen BO, Richet P (2005) *Silicate Glasses and Melts: Properties and Structure*. Elsevier, Amsterdam.
- Nagasawa H, Mourikis S, Schulke W (1989) X-ray Raman spectrum of Li, Be, and graphite in a high-resolution inelastic synchrotron X-ray scattering experiment. *J Phys Soc Japan* 58:710-717
- Nagasawa H, Mourikis S, Schulke W (1997) Momentum-transfer dependence of the near edge structure of Li. *J Phys Soc Japan* 66:3139-3146
- Nagle KP, Seidler GT, Shirley EL, Fister TT, Bradley JA, Brown FC (2009) Final-state symmetry of Na 1s core-shell excitons in NaCl and NaF. *Phys Rev B* 80:045105
- Navrotsky A (1995) Energetics of silicate melts. *In: Structure, Dynamics, and Properties of Silicate Melts*. Stebbins JF, McMillan PF, Dingwell DB (Eds.) Mineralogical Society of America, Washington, D.C. p 121-143
- Newville M (2014) Fundamentals of XAFS. *Rev Mineral Geochem* 78:33-74
- Okuno M, Reynard B, Shimada Y, Syono Y, Willaime C (1999) A Raman spectroscopic study of shock-wave densification of vitreous silica. *Phys Chem Miner* 26:304-311
- Poe BT, McMillan PF, Rubie DC, Chakraborty S, Yarger JL, Diefenbacher J (1997) Silicon and oxygen self-diffusivities in silicate liquids measured to 15 Gigapascals and 2800 Kelvin. *Science* 276:1245-1248
- Prewitt CT, Downs RT (1998) High-pressure crystal chemistry. *Rev Mineral Geochem* 37:283-317
- Price GD (2007) Mineral physics: past, present, and future. *In: Treatise on Geophysics*. Vol 2. Gerald S (Ed) 2. Elsevier, Amsterdam, p 1-6
- Rehr JJ, Albers RC (2000) Theoretical approaches to X-ray absorption fine structure. *Rev Mod Phys* 72:621-654
- Rehr JJ, Kas JJ, Vila FD, Prange MP, Jorissen K (2010) Parameter-free calculations of X-ray spectra with FEFF9. *Phys Chem Chem Phys* 12:5503-5513
- Revenaugh J, Sipkin SA (1994) Seismic evidence for silicate melt atop the 410 km mantle discontinuity. *Nature* 369:474-476
- Reynard B, Okuno M, Shimada Y, Syono Y, Willaime C (1999) A Raman spectroscopic study of shock-wave densification of anorthite (CaAl₂Si₂O₈) glass. *Phys Chem Miner* 26:432-436
- Rez P, Alvarez JR, Pickard C (1999) Calculation of near edge structure. *Ultramicroscopy* 78:175-183
- Rueff J-P, Shukla A (2010) Inelastic X-ray scattering by electronic excitations under high pressure. *Rev Mod Phys* 82:847-896
- Rueff JP, Joly Y, Bartolome F, Krisch M, Hodeau JL, Marques L, Mezouar M, Kaprolat A, Lorenzen M, Sette F (2002) X-ray Raman scattering from the carbon K-edge in polymerized C₆₀: experiment and theory. *J Phys-Condens Mat* 14:11635-11641
- Sakamaki T, Suzuki A, Ohtani E (2006) Stability of hydrous melt at the base of the Earth's upper mantle. *Nature* 439:192-194
- Sakko A, Hakala M, Soininen JA, Hamalainen K (2007) Density functional study of X-ray Raman scattering from aromatic hydrocarbons and polyfluorene. *Phys Rev B* 76:205115
- Sakko A, Rubio A, Hakala M, Hamalainen K (2010) Time-dependent density functional approach for the calculation of inelastic X-ray scattering spectra of molecules. *J Phys Chem* 133:174111

- Sakko A, Galambosi S, Inkinen J, Pylkkanen T, Hakala M, Huotari S, Hamalainen K (2011) Inelastic X-ray scattering and vibrational effects at the K-edges of gaseous N₂, N₂O, and CO₂. *Phys Chem Chem Phys* 13:11678-11685
- Sauer H, Brydson R, Rowley PN, Engel W, Thomas JM (1993) Determination of coordination and coordination specific site occupancy by electron-energy loss spectroscopy: An investigation of boron-oxygen compounds. *Ultramicroscopy* 49:198-209
- Sandi G, Song K, Carrado KA, Winans RE (1998) A NEXAFS determination of the electronic structure of carbons for lithium-ion cells. *Carbon* 36:1755-1758
- Schulke W (2007) *Electron Dynamics by Inelastic X-ray Scattering*. Oxford University Press
- Schulke W, Bonse U, Nagasawa H, Kaprolat A, Berthold A (1988) Interband-transitions and core excitations in highly oriented pyrolytic-graphite studied by inelastic synchrotron X-ray scattering: Band structure information. *Phys Rev B* 38:2112-2123
- Schulke W, Gabriel KJ, Berthold A, Schulteschrepping H (1991) Interlayer states of LiC₆ investigated by inelastic X-ray scattering spectroscopy (IXSS) using Li core excitation. *Solid State Commun* 79:657-660
- Schulke W, Nagasawa H, Mourikis S, Lanzki P (1986) Dynamic structure of electrons in Li metal: Inelastic synchrotron X-ray scattering results and interpretation beyond the random-phase approximation. *Phys Rev B* 33:6744-6757
- Schwarz K, Blaha P, Madsen GKH (2002) Electronic structure calculations of solids using the WIEN2k package for material sciences. *Comput Phys Commun* 147:71-76
- Schwarz WHE, Mensching L, Hallmeier KH, Szargan R (1983) K-shell excitation of BF₃, CF₄ and MBF₄ compounds. *Chem Phys* 82:57-65
- Seifert F, Sharp T, Poe B, Wu Z (1996) ELNES Si L-, K-edge and O K-edge spectroscopy as a tool for distinction of four- vs six-coordinated silicon in high-pressure phases. *Phys Chem Miner* 23:227-227
- Shen G, Wang Y (2014) High-pressure apparatus integrated with synchrotron radiation. *Rev Mineral Geochem* 78:745-777
- Shvyd'ko Y V, Lerche M, Kuetsgens U, Ruter HD, Alatas A and Zhao J (2006) X-ray Bragg diffraction in asymmetric backscattering geometry. *Phys Rev Lett* 97:235502
- Shimoda K, Okuno M, Syono Y, Kikuchi M, Fukuoka K, Koyano M, Katayama S (2004) Structural evolutions of an obsidian and its fused glass by shock-wave compression. *Phys Chem Miner* 31:532-542
- Soininen JA, Mattila A, Rehr JJ, Galambosi S, Hamalainen K (2006) Experimental determination of the core-excited electron density of states. *J Phys-Condens Matter* 18:7327-7336
- Song TRA, Helmberger DV, Grand SP (2004) Low-velocity zone atop the 410-km seismic discontinuity in the northwestern United States. *Nature* 427:530-533
- Stebbins JF (1995) Dynamics and structure of silicate and oxide melts: nuclear magnetic resonance studies. *Rev Mineral* 32:191-246
- Stebbins JF, Xu Z (1997) NMR evidence for excess non-bridging oxygen in aluminosilicate glass. *Nature* 390, 60-62
- Stetsko YP, Keister JW, Coburn DS, Kodituwakku CN, Consolo A, Cai YQ (2011). Multiple-wave diffraction in high energy resolution back-reflecting x-ray optics. *Phys Rev Lett* 107:155503
- Sternemann H, Soininen JA, Sternemann C, Hamalainen K, Tolan M (2007a) Near-edge structure of nonresonant inelastic X-ray scattering from L-shell core levels studied by a real-space multiple-scattering approach. *Phys Rev B* 75:075118
- Sternemann H, Sternemann C, Tse JS, Desgreniers S, Cai YQ, Vanko G, Hiraoka N, Schacht A, Soininen JA, Tolan M (2007b) Giant dipole resonance of Ba in Ba₈Si₄₆: An approach for studying high-pressure induced phase transitions of nanostructured materials. *Phys Rev B* 75:245102
- Stixrude L (2007) Properties of rocks and minerals - seismic properties of rocks and minerals, and structure of the Earth. *In: Treatise on Geophysics*. Gerald S (ed) Elsevier, Amsterdam p 7-32.
- Stixrude L, Karki B (2005) Structure and freezing of MgSiO₃ liquid in Earth's lower mantle. *Science* 310:297-299
- Stohr J (2003) *NEXAFS Spectroscopy*. Springer, New York
- Suzuki T (1967) X-ray Raman scattering experiment. I. *J Phys Soc Japan* 22:1139
- Tamura E, van Ek J, Fröba M, Wong J (1995) X-Ray absorption near edge structure in metals: relativistic effects and core-hole screening. *Phys Rev Lett* 74:4899
- Tanaka I, Mizoguchi T, Yoshiya M, Ogasawara K, Adachi H, Mo SD, Ching WY (2002) First principles calculation of ELNES by LCAO methods. *J Electron Microsc* 51:S107-S112
- Tohji K, Udagawa Y (1987) Novel-approach for structure-analysis by X-ray Raman-scattering. *Phys Rev B* 36:9410-9412
- Tohji K, Udagawa Y (1989) X-ray Raman scattering as a substitute for soft X-ray extended X-ray absorption fine-structure. *Phys Rev B* 39:7590-7594

- Tschauner O, Asimov PD, Kostandova N, Ahrens TJ, Ma C, Sinogeikin S, Liu Z, Fakra S, Tamura N (2009) Ultrafast growth of wadsleyite in shock-produced melts and its implications for early solar system impact processes. *Proc Natl Acad Sci USA* 106:13691-13695
- Tse JS, Shaw DM, Klug DD, Patchkovskii S, Vanko G, Monaco G, Krisch M (2008) X-ray Raman spectroscopic study of water in the condensed phases. *Phys Rev Lett* 100:095502
- Tsuji J, Nakamatsu H, Mukoyama T, Kojima K, Ikeda S, Taniguchi K (2002) Lithium K-edge XANES spectra for lithium compounds. *X-Ray Spectrom* 31:319-326
- Watanabe N, Hayashi H, Udagawa Y, Takeshita K, Kawata H (1996) Anisotropy of hexagonal boron nitride core absorption spectra by X-ray Raman spectroscopy. *Appl Phys Lett* 69:1370-1372
- Wernet P, Nordlund D, Bergmann U, Cavalleri M, Odelius M, Ogasawara H, Naslund LA, Hirsch TK, Ojamae L, Glatzel P, Pettersson LGM, Nilsson A (2004) The structure of the first coordination shell in liquid water. *Science* 304:995-999
- Wernet P, Testemale D, Hazemann JL, Argoud R, Glatzel P, Pettersson LGM, Nilsson A, Bergmann U (2005) Spectroscopic characterization of microscopic hydrogen-bonding disparities in supercritical water. *J Phys Chem* 123:154503
- Wilke M, Farges F, Petit PE, Brown GE Jr, Martin F (2001) Oxidation state and coordination of Fe in minerals: An FeK-XANES spectroscopic study. *Am Mineral* 86:714-730
- Wolf GH, McMillan PF (1995) Pressure effects on silicate melt structure and properties. *Rev Mineral* 32:505-562
- Wright AC, Stone CE, Sinclair RN, Umetsuki N, Kitamura N, Ura K, Ohtori N, Hannon AC (2000) Structure of pressure compacted vitreous boron oxide. *Phys Chem Glass* 41:296-299
- Wu M, Liang Y, Jiang J-Z, Tse JS (2012) Structure and properties of dense silica glass. *Scientific Reports* 2:398
- Wu ZY, Ouyard G, Gressier P, Natoli CR (1997) Ti and O K-edges for titanium oxides by multiple scattering calculations: Comparison to XAS and EELS spectra. *Phys Rev B* 55:10382-10391
- Wu ZY, Seifert F, Poe B, Sharp T (1996) Multiple-scattering calculations for SiO₂ polymorphs: A comparison to ELNES and XANES spectra. *J Phys-Condens Mat* 8:3323-3336
- Xue X, Stebbins JF, Kanzaki M, Tronnes RG (1989) Silicon coordination and speciation changes in a silicate liquid at high pressures. *Science* 245:962-964
- Xue X, Stebbins JF, Kanzaki M (1994) Correlations between O¹⁷ NMR parameters and local structure around oxygen in high-pressure silicates and the structure of silicate melts at high pressure. *Am Mineral* 79:31-42
- Yarger JL, Smith KH, Nieman RA, Diefenbacher J, Wolf GH, Poe, BT, McMillan, PF (1995) Al coordination changes in high-pressure aluminosilicate liquids. *Science* 270:1964-1967
- Yi YS, Lee SK (2012) Pressure-induced changes in local electronic structure of SiO₂ and MgSiO₃ polymorphs: Insights from ab initio calculations of O K-edge energy-loss near-edge structure spectroscopy. *Am Mineral* 97:897-909